DIFFRACTION AT HERA

Nicolò Cartiglia
Columbia University, Nevis Laboratories
136 South Broadway, Irvington, NY, 10533 USA

Representing the H1 and ZEUS Collaborations

ABSTRACT

Recent results on diffraction at HERA, as measured by the H1 and ZEUS Collaborations, are reviewed. Results on the photon-proton total hadronic cross section, on vector meson production both at small and large photon virtuality and on photon diffraction, are presented. The experimental signature of diffraction at HERA, as well as the selection methods used by the two collaborations, are explained.

Contents

1 Introduction

Photon-proton collisions have been extensively studied in fixed target experiments up to center-of-mass energies, $W_{\gamma p}$, of about 20 GeV, using both real and virtual photons. At the HERA collider at DESY, 820 GeV protons collide with 27.5 GeV electrons or positrons. The HERA physics program is very rich, ranging from nonperturbative to perturbative QCD, heavy-flavor physics, and to the measurement of the quark and gluon densities in the proton and in the photon. Two general-purpose detectors, H1 (Ref. 1) and ZEUS (Ref. 2), operate at HERA and are instrumented with high-resolution calorimeters and tracking chambers.

The results presented here have been obtained using data collected during 1994 and 1995, for a total of about 9 pb^{-1}. More detailed presentations on individual subjects can be found in many proceedings.[3]

2 Diffraction and Total Cross Section

Historically, hadronic diffraction processes and total cross sections have been described using the concept of "Pomeron exchange." The simplest way to introduce the concept of the Pomeron is within the framework of Regge theory.[4,5] Consider the example shown in Fig. 1: $\pi^- p \to \pi^0 n$ where t is the four-momentum transfer. According to quantum number conservation, this reaction might happen via the exchange of a virtual ρ^0, a_2, g hadron. If the values of the masses and spins of these particles are plotted on the right-hand side of the spin-t plane (where t is positive), they lie almost on a straight line determining a "trajectory" of particles. The general expression for a straight-line trajectory is:

$$\alpha(t) = \alpha(0) + \alpha' \cdot t,$$

where $\alpha(0)$ is the intercept and α' the slope. The most important trajectories are approximately linear with a universal slope $\alpha' = 0.9$ GeV^2; the first particle on a trajectory gives the name to the trajectory itself (in the above example, the ρ trajectory is exchanged). Regge theory predicts that the properties of a t-channel reaction (that happens on the left-hand side of the spin-t plane, where t is negative, via the exchange of off-mass shell particles), $\pi^- p \to \pi^0 n$ for example, are determined by the parameters of the trajectory formed by the exchanged particles on the right-hand side of the spin-t plane (the ρ trajectory in the case above).

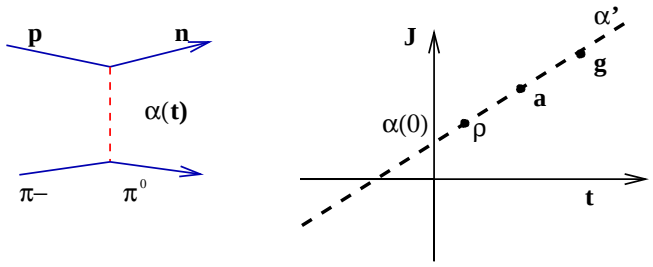

Figure 1: Schematic diagram for $\pi^- p \to \pi^0 n$ scattering and the exchanged trajectory.

Let's consider the dependence of the total cross section (a t-channel process) with the square of the center-of-mass energy s. According to Regge theory, it is parametrized as:

$$\sigma_{tot}(s) \propto \sum_k s^{\alpha_k(0)-1}, \tag{1}$$

where $\alpha_k(0) = 1, ..n$, are the intercepts of the trajectories exchanged. Using only two main trajectories, $\sigma_{tot}(s)$ for $p\bar{p}$, pp, $K^{\pm}p$, $\pi^{\pm}p$, γp have been fitted by Donnachie and Landshoff[6] with an expression of the form:

$$\sigma_{tot}(s) = Xs^{0.0808} + Ys^{-0.4525},$$

where X, Y are parameters which depend on the exchanged field. The first trajectory, called Pomeron trajectory, has intercept $\alpha_{I\!P}(0) = 1.0808$ while the second term, which represents an effective meson trajectory, has intercept $\alpha_k(0) = 0.545$. At high enough energy, only the Pomeron term is important. The Pomeron, identified as the first particle of the Pomeron trajectory, is responsible for the rise of the total cross section as a function of the center-of-mass energy. Since the bulk of the processes contributing to the total cross section has very small p_t, the Pomeron exchanged in these reactions is called a "soft Pomeron." The soft Pomeron trajectory has intercept $\alpha_{I\!P}(0) \simeq 1.08$ and slope $\alpha' \simeq 0.25$ GeV^2.

Figure 2 schematically shows three different types of diffractive reactions: elastic scattering (a), single diffraction (b), where one of the incoming particle dissociates, and double diffraction (c), where both incoming particles dissociate. In diffractive scattering, the hadronization of the final states X and Y with masses M_Y^2, M_X^2 happens independently, as shown in Fig. 2(d). If the center-of-mass energy $\sqrt{s}$ is large enough (ln(s) $\gg ln(M_Y^2) + ln(M_X^2)$), then there is a gap in rapidity between X and Y.

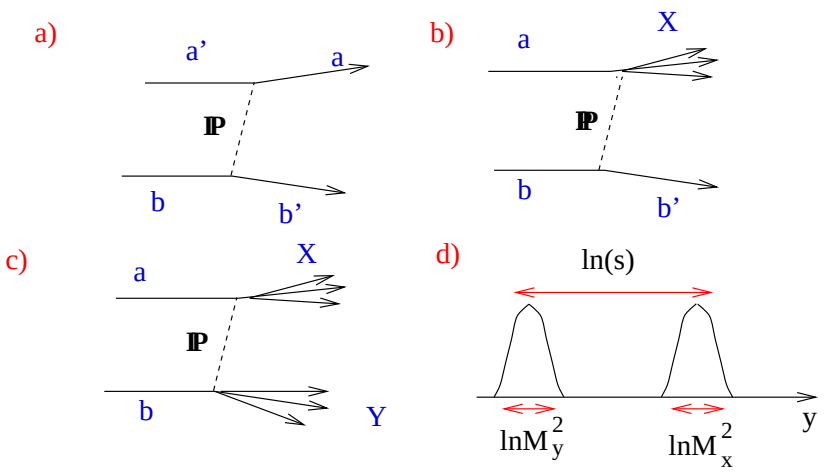

Figure 2: Diagrams for three different types of diffractive reactions: elastic scattering (a), single diffraction (b) where one of the incoming particle fragments, and double diffraction (c). (d) shows energy flow as a function of rapidity for ln(s) $\gg ln(M_Y^2) + ln(M_X^2)$.

Experiment	$W_{\gamma p}$Range	$W_{\gamma p}$
ZEUS	$167 < W_{\gamma p} < 194$	$\sigma_{tot}^{\gamma p} = 143 \pm 4 \pm 17$ μb
H1	$< W_{\gamma p} >$=200	$\sigma_{tot}^{\gamma p} = 165 \pm 2 \pm 11$ μb

Table 1: Summary of experimental results on the measurements of σ_{tot} at HERA.

3 Total Cross Section at HERA

The values of the total hadronic γp cross section at HERA as measured by the H1 (Ref. 7) and ZEUS (Ref. 8 Collaborations are shown in Fig. 3 together with a compilation of low-energy results. The Donnachie and Landshoff parametrizations including (dotted line) or not (solid line) recent CDF (Ref. 9 results and the ALLM (Ref 10 parametrization (dashed line) are also shown. The HERA data are in agreement with these predictions, and therefore, with the assumption that also at HERA "soft" Pomeron exchange is responsible for the increase of $\sigma_{tot}^{\gamma p}$as a function of the center-of-mass energy.

The diffractive cross section represents a large fraction of the total cross section: at HERA, for example, the diffractive and nondiffractive parts are, according to the H1 Collaboration,[7] $\sigma_{dif}^{\gamma p} = 69.2 \pm 13.2$ μb and $\sigma_{non-dif}^{\gamma p} = 96.1 \pm 17.9$ μb,

giving $\sigma_{dif}/\sigma_{tot} = (42 \pm 8)\%$, while according to the ZEUS Collaboration,[8] $\sigma_{dif}/\sigma_{tot} = (36 \pm 8)\%$.

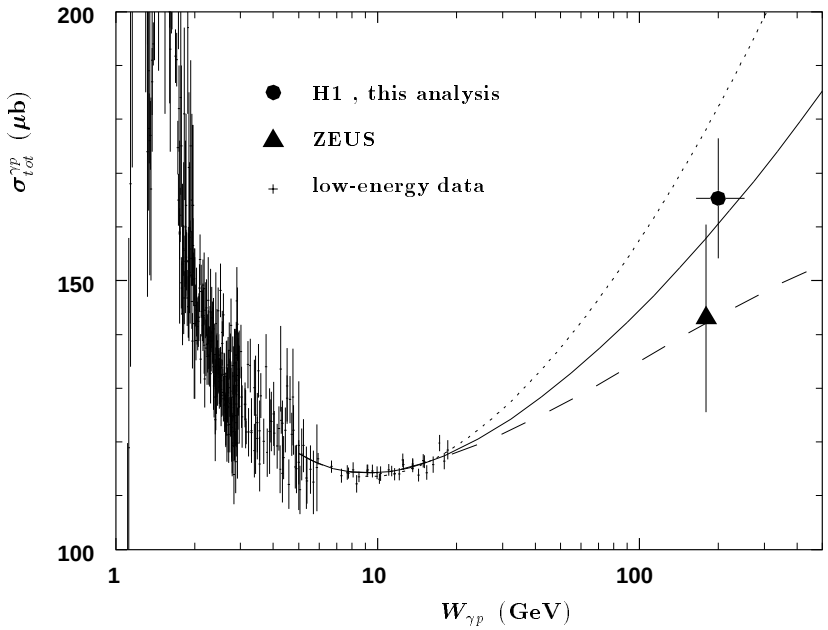

Figure 3: Total γp cross section as a function of $W_{\gamma p}$. The results are shown together with two parametrizations from Donnachie and Landshoff that include (dotted line) or not (solid line) recent CDF results and with the ALLM parametrization (dashed line).

4 Kinematics of Diffractive Events at HERA

In Fig. 4, a diagram for diffractive ep scattering is shown. A photon $\gamma^*(Q^2)$ with virtuality $-q^2 = Q^2$ is emitted at the electron vertex*. Depending on the value of Q^2, the events are divided into two large families: photoproduction, for $Q^2 < 4$ GeV^2, and deep inelastic scattering (DIS), for $Q^2 > 4$ GeV^2. $s = (k+p)^2$ is defined as the center-of-mass energy squared of the ep system while ${W_{\gamma p}}^2 = (q+p)^2$ is used to indicate the center-of-mass energy of the virtual photon-proton (γp) system. At large Q^2, in the frame where the proton has infinite momentum, the variable $x_{Bj} = \frac{Q^2}{2p\cdot q}$ represents the fraction of the proton longitudinal momentum carried by the struck quark. In the proton rest frame, $y = Q^2/(sx_{Bj})$ equals the

*The symbol γ is used for quasireal photons while the symbol γ^* is used for virtual photons.

fraction of the electron energy transferred to the proton.

In addition, diffractive events are described by the following variables: t, the square of the four-momentum transfer at the proton vertex, and $x_{I\!P}$, the momentum fraction of the Pomeron in the proton.

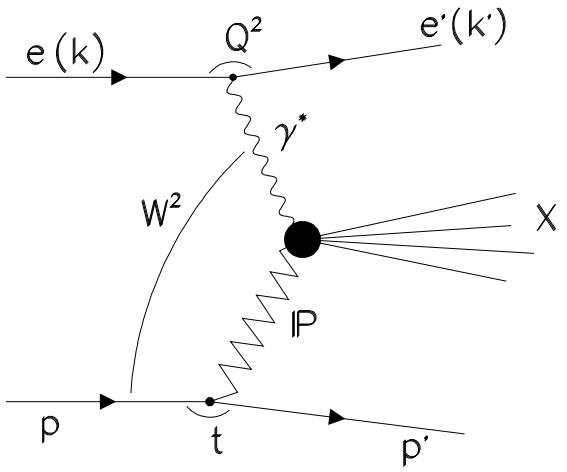

Figure 4: Diagram for diffractive scattering at HERA.

If the reaction is elastic or single diffractive (or photon diffraction as sometimes single diffraction is called for the HERA regime), then the quantities t and $x_{I\!P}$ can be determined either from the scattered proton or from the system M_X .

If the longitudinal and transverse momentum of the scattered proton, $p'_z, p'_\perp$, are measured, then $x_{I\!P}$and t are calculated as:

$$x_L \simeq p'_z/E_p \longrightarrow x_{I\!P} = 1 - x_L \tag{2}$$

$$t = (P - P')^2 \simeq -\frac{(p'_\perp)^2}{x_L} - m_p^2 \frac{(1 - x_L)^2}{x_L} \quad , \tag{3}$$

where m_p is the proton mass. If the proton is not observed, a measurement of $x_{I\!P}$can be obtained as: beginequation $x_{I\!P}$= (P-P$\frac{{}')\cdot q}{P\cdot q \simeq \frac{M_X^2+Q^2}{W^2+Q^2-m_p^2}}$where M_X is .(3)

the mass of the system X. t can be reconstructed from the system X only for some exclusive reactions, such as vector meson production, where the resolution on $p'_\perp$ is accurate enough.

5 Experimental Signature of Diffraction at HERA

One of the main issues concerning diffraction at HERA is the experimental method to separate diffractive from nondiffractive events. For some exclusive reactions, the distinction is actually quite easy. Let's consider, for example, exclusive ρ^0 production and decay:

$$\gamma p \longrightarrow \rho^0 p$$
$$\rho^0 \longrightarrow \pi^+\pi^-.$$

The central detector is empty, except for the two tracks coming from the ρ^0 decay. This topology is very unusual and the background from "non-Pomeron" exchange is negligible. Inclusive γ diffraction, $\gamma p \to Xp$, is on the other hand more difficult to identify. Two quantities can help in the distinction: a rapidity gap in the final state particle production and/or the presence of a highly energetic scattered proton.

5.1 Rapidity Gaps

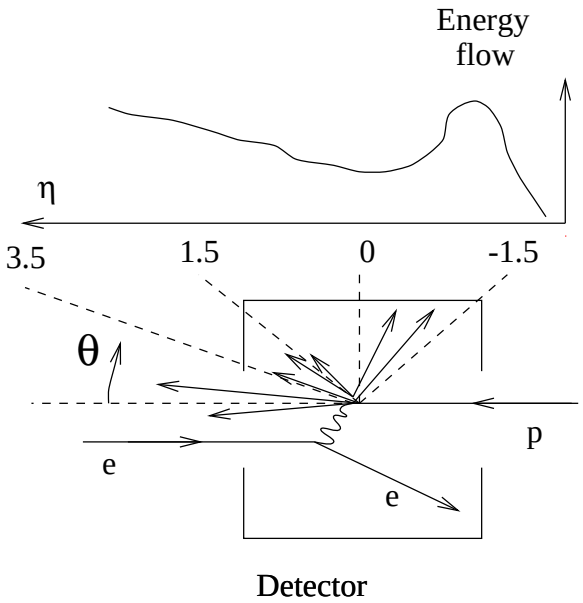

Figure 5: Energy flow vs η for nondiffractive ep scattering at HERA.

Figure 5 schematically shows the energy flow as a function of pseudorapidity η for nondiffractive ep scattering at HERA[†]. Aside from the recoil electron, two main

[†]The pseudorapidity η is defined as: $\eta = -ln(tan(\theta/2))$. Following the HERA convention, the angle θ is measured with respect to the proton beam direction.

groups of particles can be identified: particles produced at high rapidity in the hadronization of the proton remnant, and particles produced in the hadronization of the photon-parton system, typically at small or negative rapidity. In deep inelastic scattering, for example, the struck parton is deflected and emerges from the proton remnant at an angle θ_q. It is useful to express this angle as the difference in pseudorapidity between the struck parton and the proton remnant:

$$\Delta\eta = \eta_{proton\ remnant} - \eta_{\ parton}. \tag{4}$$

Since the pseudorapidity interval covered by a system with center-of-mass energy $\sqrt{s}$ is given by:

$$\Delta\eta \sim ln(\frac{s}{m_p^2}) \tag{5}$$

with m_p the proton mass, then we can show that the pseudorapidity interval between the proton remnant and the struck quark is:

$$\Delta\eta \sim ln(\frac{{W_{\gamma p}}^2}{m_p^2}) - ln(\frac{x_{Bj}{W_{\gamma p}}^2}{m_p^2}) \sim ln(\frac{1}{x_{Bj}}), \tag{6}$$

where $ln(\frac{W_{\gamma p}x^2}{m_p^2})$ is the total rapidity covered by the γ-p system and $ln(\frac{x_{Bj}W_{\gamma p}^2}{m_p^2})$ is the amount covered by the γ-struck quark system. Due to the color string connecting the struck parton and the proton remnant, the rapidity gap $\Delta\eta$ is filled with particles in the hadronization process. In particular as x_{Bj} decreases, the average hadron multiplicity $< n_h >$ increases faster than the pseudorapidity interval $\Delta\eta$, making it less and less likely for rapidity gaps to be visible.[13] If we assume the produced hadrons to fill the rapidity gap according to a Poisson distribution, the probability w_{gap} to have no particles in the gap $\Delta\eta$ has the form:

$$w_{gap} \sim e^{-<n_h>} < e^{-\Delta\eta}. \tag{7}$$

This expression means that rapidity gaps between the proton fragments and the jet produced by the struck quark are exponentially suppressed. For Reggeon or Pomeron exchange, Fig. 6, the probability to have a rapidity gap $\Delta\eta$ depends on the intercept of the exchanged trajectory.[14]

$$p(\Delta\eta) \sim e^{-2(\alpha(0)-1)\Delta\eta}.$$

Let's then consider different possibilities:

*I*P exchange: $\alpha_{I\!P}(0) \sim 1 \quad \Rightarrow \quad p(\Delta\eta) \sim e^0$

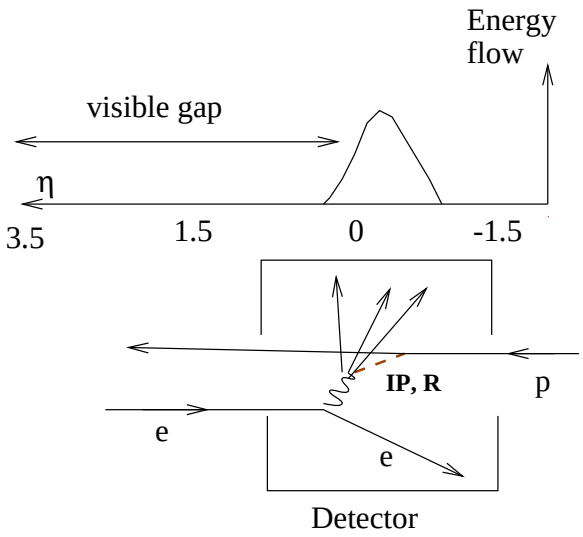

Figure 6: Energy flow vs η for diffractive ep scattering at HERA.

ρ, a_2, f_2, ω exchange: $\alpha_R(0) \sim 0.5 \quad \Rightarrow \quad p(\Delta\eta) \sim e^{-\Delta\eta}$

π exchange: $\alpha_\pi(0) \sim 0 \quad \Rightarrow \quad p(\Delta\eta) \sim e^{-2\Delta\eta}$.

Therefore, even though ρ, π, *and* $I\!P$ are colorless exchanges, only $I\!P$ exchange produces rapidity gaps that are not suppressed as the gap width increases. It is therefore possible to operationally define diffraction[15] by the presence of a rapidity gap: diffractive events are those which lead to a large rapidity gap in final state phase space and are not exponentially suppressed as a function of the gap width.

5.2 Leading Proton in the Final State

In diffractive events, the incoming beam particles, when they do not dissociate, conserve a large fraction of their initial momentum. At HERA, the diffractively scattered proton carries on average more than 99% of its initial momentum. The cross sections for nondiffractive processes to produce suchenergetic protons is very small compared with the diffractive cross section making the detection of a high-energy proton a clean tag for diffractive physics. Figure 7 schematically shows the spectra of leading protons generated from different mechanisms: at $x_L \simeq 1$, single diffraction is almost the sole component, while moving away from $x_L = 1$, double diffraction and reggeon exchange become important. Traditionally, $x_L = 0.9$ has been used to indicate the x_L value at which the diffractive and non-diffractive part of the spectrum are equal. Leading protons can also be produced in "standard" DIS events as part of the proton remnant jet, but they have on

average a much lower x_L value. A recent release of the LEPTO MonteCarlo,[16] on the other hand, includes leading proton production in the fragmentation of the proton remnant with a cross section comparable to reggeon exchange. Note that the distinction between the different mechanisms for leading proton production is somehow arbitrary and there might be a lot of overlap.

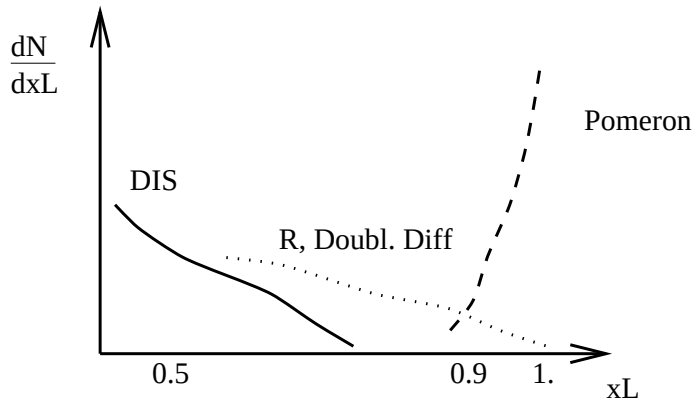

Figure 7: Spectra of leading protons generated from different mechanisms: Pomeron exchange (dashed line), reggeon exchange and double diffraction (dotted line), and "standard DIS" (solid line) as a function of x_L.

In the transverse plane, leading protons have rather small momentum, with a typical $p_\perp^2$ distribution of the form:

$$\frac{dN}{dp_\perp^2} \sim e^{-b \cdot p_\perp^2}$$

with b = 5-15 GeV^{-2}. This feature makes their detection quite difficult since they tend to stay very close to the beam line. Because of this, movable sections of the beam pipe, called "Roman pots," are used by both the H1 and ZEUS Collaborations to allow the insertion of high-precision detectors down to a few centimeters from the beam line.

6 Models for Diffractive $\gamma^* p$ Scattering

Several models have been proposed to explain diffractive interactions in ep scattering. In some instances, a connection is made between Regge concepts (like Pomerons) with QCD concepts (like gluons). Here we present a brief description of some of the ideas on which the models are based.

- Factorization of vertices and Pomeron structure function: Factorization considers the IPp vertex as independent of the $IP\gamma^*$ interaction. A universal Pomeron flux factor $f_{IP/p}(x_{IP},t)$ characterizes the IPp vertex, and parametrizations obtained from fits to pp and p$\bar{\text{p}}$ diffractive data can be used in ep collisions. Several different expressions for $f_{IP/p}(x_{IP},t)$ have been proposed[17–19] which all include an exponential dependence on t of the type $e^{-b|t|}$ with b $\sim$ 5-8 GeV^{-2} and a dependence on the Pomeron longitudinal momentum x_{IP} of the type $\sim 1/x_{IP}$. These models express the diffractive γ^* p cross section as

$$\sigma^{\gamma^* p}(Q^2,\beta,x_{IP},t) \propto f_{IP/p(x_{IP},t)} \cdot \sigma^{\gamma^* IP}(Q^2,\beta) \quad , \tag{8}$$

and describe deep inelastic γ^*p and $\gamma^* IP$ interactions in the same way: the incoming γ^* interacts with one component of the target, leaving behind a remnant. For $\gamma^* IP$ interaction, the scaling variable that plays the same role of x_{Bj} is:

$$\beta = \frac{Q^2}{2x_{IP}p_{proton}\cdot q} \sim \frac{Q^2}{M_X^2+Q^2} \quad . \tag{9}$$

The $\gamma^* IP$ cross section can then be written as:

$$\sigma_{tot}^{\gamma^* IP}(Q^2,\beta) = \frac{4\pi^2\alpha_{em}}{Q^2} F_2^{IP}(Q^2,\beta) \quad , \tag{10}$$

where $\mathrm{F}_2^{IP}(Q^2,\beta)$ is the Pomeron structure function; i.e., the probability for finding a quark of fractional momentum β in the Pomeron.

- Factorization breaking and effective Pomeron structure function: The diffractive ep interaction is viewed as photon diffractive dissociation on the proton (some examples are given in Refs. 20–24). Consider ep scattering in the proton rest frame. Upstream of the proton, Fig. 8, the incoming γ (or γ^*) fluctuates into different hadronic states, and its wave function can be expressed as:

$$|\gamma> = |\gamma>_{bare} + |q\bar{q}> + |q\bar{q}g> + ...$$

. The Pomeron, viewed as two gluon-exchange, couples to these hadronic states in an s-channel interaction, and, technically, there is no $\mathbb{P}$ remnant since both gluons interact with the photon. In this approach, the virtual photon couples with more than one Pomeron constituent and the meanings of β and $\mathrm{F}_2^{IP}(Q^2,\beta)$ are not well-defined in terms of partons; in particular, factorization is not a natural consequence. To compare the predictions from this approach to those of the

previous type of model, an effective $\mathbb{P}$ structure function, $F_{2\,eff.}^{IP}(Q^2,\beta)$, is introduced. In this picture, the interaction of the $q\bar{q}$ state generates a different value of $\alpha_{I\!P}$ than the interaction of the $q\bar{q}g$ state[25] with an effective $\alpha_{I\!P}$ increasing at small $x_{I\!P}(x_{I\!P} \simeq 10^{-4})$. Therefore, the $q\bar{q}$ and $q\bar{q}g$ fluctuations have different Pomeron fluxes breaking the factorization mechanism. According to Ref. 26, factorization is also broken by the exchange of longitudinal photons. The states are characterized by the transverse and longitudinal momentum $(k_\perp, z)$ of the $q\bar{q}$pair (taken as an example) and by the quark mass (m_q). The radius $r_\perp^2$ of the state depends on the inverse of $k_\perp^2 \cdot Q^2$ and m_q^2:

$$\frac{1}{r_\perp^2} \propto \frac{k_\perp^2 \cdot Q^2}{M_X^2}$$

$$\frac{1}{r_\perp^2} \propto m_q^2.$$

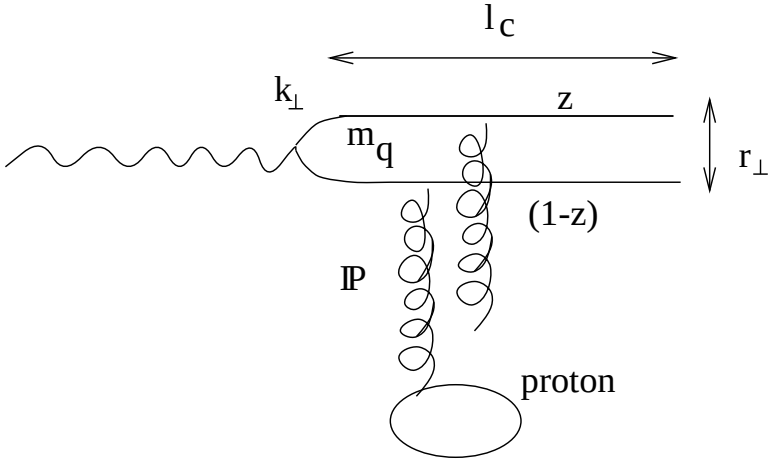

Figure 8: Diffractive γp scattering in the proton rest frame.

If the state has large $r_\perp^2$, both $k_\perp^2 \cdot Q^2$ and m_q^2 are small. In this case, the gluon-quark coupling is large, and pQCD cannot be applied since the photon acts like an extended object providing no information on the microscopic nature of the interaction. Large size fluctuations are thought to be responsible for the rise of the total hadronic cross section with energy and represent the bulk of diffractive events. Large $r_\perp^2$ configurations have small $k_\perp$, and the final state particles tend to be aligned along the photon-Pomeron axis. This phenomenology is known as the Aligned Jet Model.[27]

Conversely, if $r_\perp^2$ is small either because $k_\perp^2 \cdot Q^2$ (high Q^2DIS events) or m_q^2 (production of charm or bottom $q\bar{q}$pair) is large, then the gluon-quark coupling is small and pQCD can be applied.

- **Soft color interaction:** in this model,[28] diffractive scattering is viewed as dominated by the exchange of one "hard" gluon plus nonperturbative color interactions to allow a color singlet final state.

7 Vector Meson Production: $\gamma p \rightarrow$Vp

In the range of center-of-mass energy $W_{\gamma p}$up to 20 GeV covered by pre-HERA experiments, this process has been described very successfully within the framework of the Vector Dominance Model (VDM).[29] In this model, the photon is assumed to fluctuate into a virtual vector meson which then interacts elastically with the proton via the exchange of a Pomeron, Fig. 9(a). From VDM, one expects:

$$\sigma^{\gamma p \rightarrow V p} = \frac{4\pi\alpha}{f_V^2}\sigma^{V p \rightarrow V p} \quad , \tag{11}$$

where $f_V^2/4\pi$ is the photon-vector meson coupling constant, which expresses the fact that the γp cross section should behave as a hadronic cross section. Since vector meson production represents the elastic part of $\sigma_{tot}^{\gamma p}$, we can use the optical theorem to relate the two cross sections at t = 0 GeV^2:

$$(\frac{d\sigma^{\gamma p \rightarrow V p}}{dt})_{t=0} = A \cdot \sigma_{tot}^2 \quad , \tag{12}$$

with A=constant. Then we can express the elastic cross section at any t value as:

$$\frac{d\sigma^{\gamma p \rightarrow V p}}{dt}(t) = (\frac{d\sigma^{\gamma p \rightarrow V p}}{dt})_{t=0} \cdot e^{f(t)} = A \cdot \sigma_{tot}^2 \cdot e^{f(t)} \quad , \tag{13}$$

where $f(t)$ is the functional dependence of the cross section on t. For vector meson production, according to Regge theory, f(t) can be written as:

$$f(t) = t \cdot (b_0 + 2\alpha'_{I\!P} \cdot ln({W_{\gamma p}}^2/W_0^2)) \quad , \tag{14}$$

where b_0 *and* W_0^2 are parameters. Using Eq. 14 into Eq. 13, integrating over t, and writing explicitly the dependence from the center-of-mass energy $W_{\gamma p}$, we obtain:

$$\sigma^{\gamma p \rightarrow V p}(W_{\gamma p}) \propto \frac{({W_{\gamma p}}^2)^{2\cdot(\alpha_{I\!P}(0)-1)}}{b_0 + 2\alpha'_{I\!P} \cdot ln({W_{\gamma p}}^2/W_0^2)} \simeq {W_{\gamma p}}^{0.22}. \tag{15}$$

It is very important to note that this reasoning is based on the assumption, supported by pre-HERA data, that the same underlying exchange governs both the total and vector meson cross section.

Recent papers (Refs. 30–32 have shown that the situation at HERA, given the large value of $W_{\gamma p}$, might be qualitatively different if a hard scale is present in the interaction. Under these circumstances, the process is calculable in QCD. The approach outlined in Sec. 6 is used: the photon fluctuates into a $q\bar{q}$pair which first interacts with the target and then the meson is formed, Fig. 9(b). The

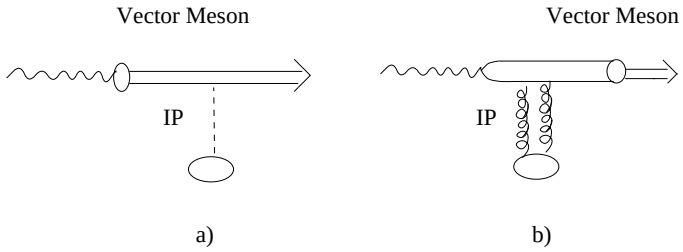

Figure 9: Different models for $\gamma p \to Vp$: (a) vector meson dominance, (b) photon diffraction.

scale of the interaction is given by the reciprocal of the fluctuation radius $r_\perp^2$, and therefore, if either $k_\perp^2 \cdot Q^2$, t, or m_q^2 is large, the process is hard. Since the transverse momentum $k_\perp^2$ generated at the photon-quark vertex is different for longitudinally and transversely polarized photons, with $\sigma^{\gamma_L \cdot p}$ dominated by large $k_\perp^2$ and $\sigma^{\gamma_\perp \cdot p}$ dominated by small $k_\perp^2$, early papers dealt only with the former photon polarization. Lately,[33] predictions for $\sigma^{\gamma_\perp \cdot p}$ have also been made.

The pQCD approach has been used to calculate the magnitude and energy dependence of the cross section for photoproduction of J/ψ mesons,[30] where the charm mass ensures a hard scale, and production of ρ^0 mesons at high (Ref. Q^2 31. In both cases, the $q\bar{q}$pair resolves the gluonic contents of the proton giving a cross section proportional to the proton gluon distribution squared[‡]:

$$\sigma^{Vp} \propto [\alpha_s(\bar{q}^2)\bar{x}g(\bar{x},\bar{q}^2)]^2 \quad . \tag{16}$$

The energy dependence is therefore no longer determined by the Pomeron intercept but by the rise of the gluon distribution at low x_{Bj}.

[‡]The square comes trivially from the fact that the Pomeron is made of two gluons.

VM Decay Mode	$Q^2 \simeq 0$ GeV^2	Ref.	$Q^2 > 0$ GeV^2	ref.
$\rho^0 \longrightarrow \pi^+ \pi^-$	X	34–36,44	X	37,38,45,46
$\phi \longrightarrow k^+ k^-$	X	39	X	40,46,47
$J/\Psi \longrightarrow \mu^+ \mu^-,\ e^+e^-$	X	41–43	X	38,46
$\omega \longrightarrow \pi^+ \pi^- \pi^0$	X	49		
$\Psi(2S) \longrightarrow \pi^+ \pi^- J/\Psi$	X	50		
$\rho^{'} \longrightarrow \pi^+ \pi^- \pi^+ \pi^-$			X	51

Table 2: List of decay modes used to identify vector meson production $\gamma p \to Vp$ at HERA.

7.1 Experimental Signature and Selection Methods for $\gamma p \to Vp$

Vector meson production is characterized by very little activity in the detector since only the vector meson decay products, and, for the DIS case, a scattered electron, are present. The processes studied so far by the two collaborations are[§] General requirements common to the analyses dealing with vector meson production are:

- predictable number of tracks for a given reaction,
- energy clusters in the calorimeter matching the track momenta, with a maximum unmatched energy of $\sim 0.5 - -1$ GeV (determined by resolution),
- $W_{\gamma p}$range restricted to 40–140 GeV. For small (large) $W_{\gamma p}$values, the tracks are too forward (backward) to be measured in the tracking chamber. For some analyses, higher values of $W_{\gamma p}$have been achieved using events with the vertex displaced in the forward direction and/or using the calorimeter.

The main sources of systematic errors come from uncertainty on the trigger thresholds, input Monte Carlo distributions, track reconstruction, uncertainties in the mass fit (in particular, for the ρ^0 analysis), nonresonant background subtraction, and magnitude of the double dissociation contribution. This last contribution is of particular interest since very little is known about double diffractive production of vector mesons. Figure 10 shows the contamination mechanism: if the mass M_Y of the excited proton system is small ($\leq$1.6 GeV for H1, $\leq$ 2 GeV for ZEUS depending on each detector forward coverage), the event looks elastic and is included in

[§]References from Ref. 44 to 51 are contributions to ICHEP 1996, Warsaw. listed in Table 2.

the sample. On the contrary, if M_Y is large, energy deposition in the calorimeter can be used as a veto. The CDF Collaboration[52] measured the mass spectrum of the system Y in $p\bar{p}$ diffraction to be $dN/dM_Y^2 = 1/M_Y^n$ with n = 2.2. This result, however, has not been obtained in the very low mass region and therefore should be used only as an indication. A more direct method used by both the H1 and ZEUS Collaborations is to model the visible energy deposition due to high M_Y states as a function of n to determine which value fits the data best and use it to perform the background subtraction.

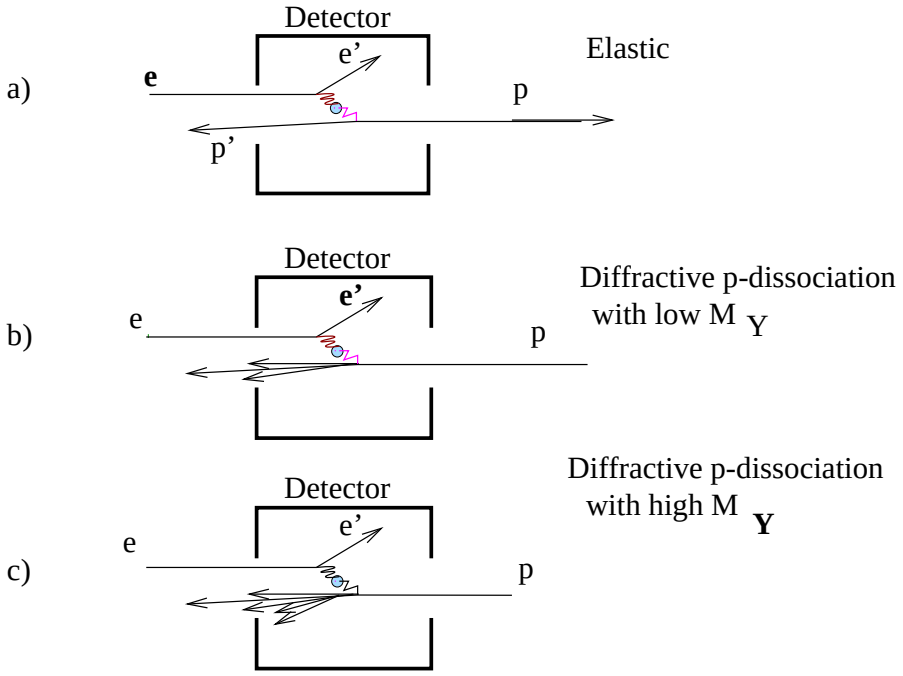

Figure 10: Double dissociation background to single dissociation. (b) If the mass M_Y of the excited proton system is small, the event looks like single diffraction and is included in the sample of elastic vector meson production. (c) For large M_Y, energy deposition in the calorimeter can be used as a veto.

7.2 Light Vector Meson Production at $Q^2 = 0$

The energy dependence of the total cross sections for light mesons (ρ^0, ω, ϕ) and J/ψ photoproduction, as measured by ZEUS and H1, are shown in Fig. 11. The Regge theory prediction $\sigma^{\gamma p \to V p}(W_{\gamma p}) \propto W_{\gamma p}^{0.22}$ is clearly supported by the data. A

summary of experimental results on the measurements of $\sigma_{tot},\ b,\ and\ r_{00}^{04}$ in photoproduction is given in Table 3. The b values are consistent with parametrizations of low-energy data and with the "shrinkage mechanism" expected in Regge theory. This mechanism predicts that the value of the slope parameter b increases as a function of the center-of-mass energy like $b(W_{\gamma p}^2) = b_0 + \ 2\alpha'_{I\!P} ln(W_{\gamma p}^2)$ where both $\alpha'_{I\!P}$ and b_0, the slope parameter at $W_{\gamma p} = 1$ GeV^2, need to be determined experimentally. This mechanism is called "shrinkage" since as b grows, the area underneath the curve $e^{b\cdot t}$ decreases considering a fixed intercept.

As the experimental results become more precise, it is possible to look for deviations from the pure exponential behavior $d\sigma/dt \sim e^{bt}$ of the t distribution. An exponential with a quadratic term[53] seems to give a good representation of the t dependence for the elastic cross section of many hadronic reactions:

$$\frac{d\sigma}{dt} = A \cdot e^{b\cdot t + c\cdot t^2}, \tag{17}$$

where c is called "curvature." The local slope parameter, defined as:

$$b(t) = \frac{d}{dt}(ln\frac{d\sigma}{dt}) = b + 2ct \tag{18}$$

is a decreasing function of t. An example is given in Fig. 12 for the case of the ρ^0 meson. Fits to hadronic scattering data yield to very similar results: b = 11.7 GeV^{-2} and c = 3.16 GeV^{-4} for pp scattering and b = 9.9 GeV^{-2} and c = 3.47 GeV^{-4} for πp scattering measured at s = 400 GeV^2 in the interval $0.02 < |t| < 0.66$ GeV^2. The common behavior of the cross section as a function of t is due to the very similar hadronic form factors for pion, proton, and photon.

The parameter b has been recently measured by the ZEUS Collaboration in ρ^0 photoproduction using data from the Leading Proton Spectrometer.[54] This is the first diffractive cross-section measurement at HERA in which the forward scattered proton is detected and its momentum measured. This makes possible a direct determination of the squared four-momentum t exchanged at the proton vertex. The LPS consists of silicon μ-strip detectors placed close to the proton beam by means of re-entrant Roman pots and detects forward-going protons scattered at angles $\leq$1 mrad. The momentum of the proton is measured using the elements (quadrupoles and dipoles) of the proton beam line, and it is reconstructed with a resolution of $\Delta p/p \simeq$0.3% at $p \simeq 820$ GeV/c. The total systematic error on the measurement of b in this analysis is 11%, the main source being the uncertainty on the acceptance ($\sim$ 7%), and the uncertainty coming from the unfolding of

Reaction	Collab.	$\sigma(\mu\text{b})$	b(GeV^{-2})	r_{00}^{04}
$\gamma p \to \rho^0 p$	ZEUS	$14.7 \pm 0.4 \pm 2.4$	$10.4 \pm 0.6 \pm 1.1$	0.055 ± 0.028
$\gamma p \to \rho^0 p$	ZEUS_{LPS}	$5.8 \pm 0.3 \pm 0.7$	$9.9 \pm 0.8 \pm 1.1$	
$\gamma p \to \rho^0 p$	H1	$9.1 \pm 0.9 \pm 2.5$	$10.9 \pm 2.4 \pm 1.1$	-0.11 $\pm$ 0.12
$\gamma p \to \rho^0 X$	ZEUS_{LPS}		$5.3 \pm 0.8 \pm 1.1$	
$\gamma p \to \omega p$	ZEUS	$1.2 \pm 0.1 \pm 0.2$	$10.0 \pm 1.2 \pm 1.4$	0.11 ± 0.08
$\gamma p \to \phi p$	ZEUS	$0.96 \pm 0.19 \pm 0.2$	$7.3 \pm 1.0 \pm 0.8$	-0.01 $\pm$ 0.04

Table 3: Summary of experimental results on the measurements of σ_{tot}, b, *and* r_{00}^{04} in photoproduction. The b values are determined using a single exponential fit $d\sigma/dt \sim e^{bt}$. The cross section $\gamma p \to \rho^0 p$ measured by the LPS is for a restricted t range.

the beam transverse momentum spread ($\sim$ 7%). It should be noted that the uncertainty coming from the proton dissociation background is negligible, when compared to analyses which do not make use of the LPS: for LPS tagged events, the contamination has been estimated to be $0.21 \pm 0.15\%$, while a previous ZEUS result estimated the contamination to be $11 \pm 6\%$. Tagging with the LPS, a leading proton with a value of x_L <0.97 has also allowed us to select a clean sample of photoproduction double diffractive ρ^0 events, $\gamma p \to \rho^0 X$. Using the transverse momentum from the decay pions, the slope parameter b has been determined to be $b_{LPS}^{\gamma p \to \rho^0 X} = 5.3 \pm 0.8 \pm 1.1$ GeV^{-2}. Figure 13 and Table 3 show the results for both single and double diffraction.

Fixed target experiments showed, at much lower $W_{\gamma p}$, that vector mesons retained the helicity of the photon (s-channel helicity conservation, SCHC). This effect was also investigated at HERA. The results can be expressed in terms of the r_{00}^{04} spin-density matrix element which gives the probability for the meson to have zero helicity. As shown in Table 3, all the measurements are consistent with a zero value for r_{00}^{04}, as required by SCHC.

7.3 Vector Meson Production with a Hard Scale

In contrast to the previous results, the cross sections for J/ψ photoproduction and light vector meson production at high Q^2show a significant rise with $W_{\gamma p}$. In particular, for the J/ψ case, the rise is clearly visible within the range of HERA data, while for the light vector mesons, the rise is observed in comparison with

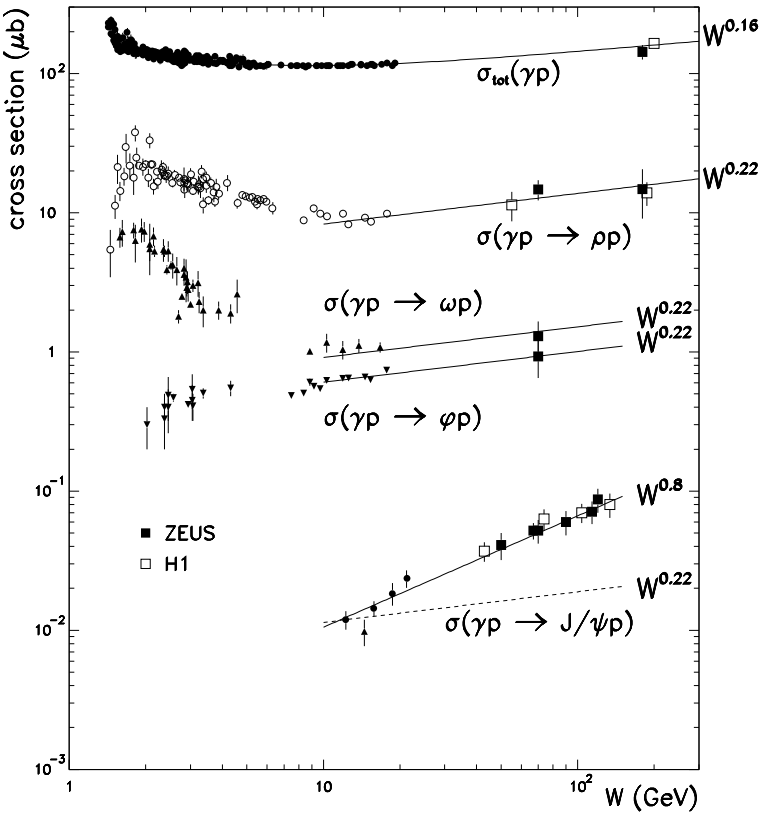

Figure 11: Total and elastic vector meson photoproduction measurements as a function of $W_{\gamma p}$. The curve overlapped to σ_{tot} is the DL parametrization ${W_{\gamma p}}^{0.16}$. The other lines are curves of the form ${W_{\gamma p}}^{0.22}$ and ${W_{\gamma p}}^{0.80}$.

lower energy data. Figure 11 and Fig. 14 show the effect for the J/ψ and ρ^0 case. The rise is inconsistent with the $W_{\gamma p}^{0.22}$ dependence used in the parametrizations of low-energy hadronic data. The measured behavior can be described instead by perturbative QCD models if a rise at small x_{Bj} of the gluon momentum density in the proton is assumed. Both the shape of the rise and the normalization could in principle be used to discriminate between models of the gluon distributions, but since the latter suffers from large theoretical uncertainty, only the shape is used. Figure 15 shows the experimental results and the expectation based on different gluon parametrizations for the ρ^0 cross section as a function of x_{Bj} in four different Q^2bins. The comparison is still dominated by experimental errors, but since the parametrizations are quite different, potentially this approach can be an invaluable tool to rule out many of the current options.

These results show that the cross section for vector meson production in the

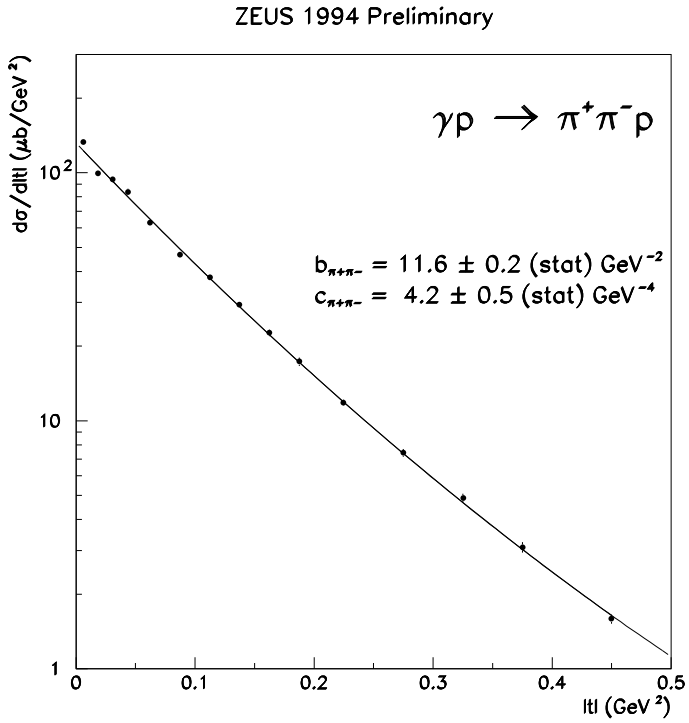

Figure 12: Measurement of the slope parameter for the reaction $\gamma p \to \rho^0 p$. A quadratic function in t, $\frac{d\sigma}{dt} \propto e^{bt+ct^2}$, was used in the fit.

presence of a hard scale has a steeper energy dependence than the total hadronic γp cross section.

7.3.1 Slope Parameter b and $R = \sigma_L/\sigma_T$ vs $W_{\gamma p}$and Q^2

The slope parameter b is related to the effective radius of the interaction R by:

$$R = \sqrt{R_p^2 + R_{VM}^2} \simeq 0.3\, b^{1/2} \;\; fm \tag{19}$$

with R_p and R_{VM} the proton and vector meson radius. Given a value of $R_p \simeq$ 0.7 fm, the effective vector meson radius in photoproduction, according to Table 3, changes from $R_{VM} \simeq 1.1$ fm for the ρ^0 meson to $R_{VM} \simeq 0.4$ fm for the ϕ meson.

The value of b varies with the meson mass, the photon virtuality Q^2, and the square of the four-momentum transfer t. Figure 16 shows a compilation of the measurements done by both H1 and ZEUS as a function of $Q^2 + M_{VM}^2$. The data show a clear trend toward small b values as $Q^2 + M_{VM}^2$ increases. Note that some authors[55] use an "effective Q^2" instead of the measured $Q^2$to set the scale. The drop of b from b $\simeq$ 10 to b $\simeq$ 4-5 GeV^{-2} implies that the size of

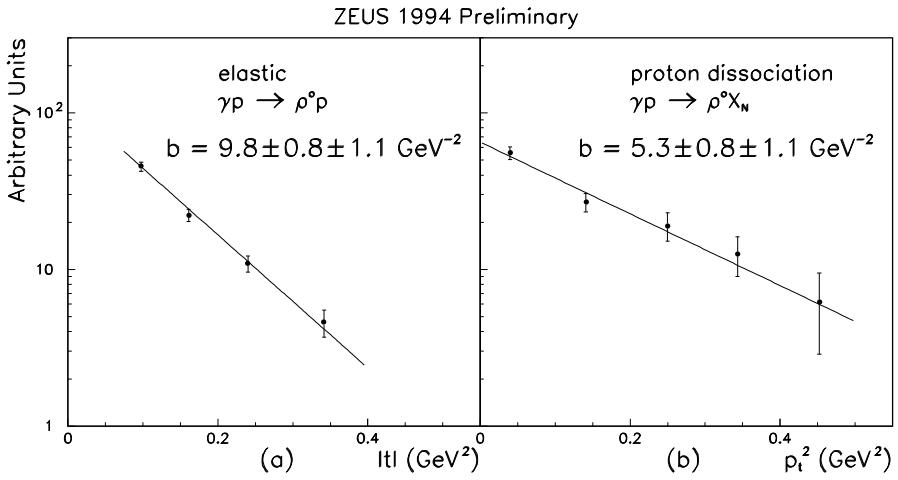

Figure 13: (a) Slope parameter b for the reaction $\gamma p \to \rho^0 p$ as obtained from the measurement of the scattered proton. The value b=9.8 has been modified to b=9.9 in the final analysis. (b) Slope parameter b for the reaction $\gamma p \to \rho^0 X$ obtained by tagging a low-energy proton in the LPS and measuring p_t^2 in the tracking chamber.

the system (the $\gamma^* \to \rho^0$ Pomeron vertex) decreases with $Q^2 + M_{VM}^2$, and that for large $Q^2 + M_{VM}^2$, we do have a short-distance interaction to justify the use of pQCD. The value b $\simeq$ 4–5 GeV^{-2} is approximately equal to what is expected from the size of the proton.

Both the H1 and ZEUS Collaborations have studied the ratio between the longitudinal and transverse cross section for ρ^0 production, $R = \frac{\sigma_L}{\sigma_T}$, as a function of Q^2. A compilation of the results is shown in Fig. 17. The photon polarization, completely transverse at Q^2=0 GeV^2, becomes more longitudinal as Q^2increases. Different QCD calculations have been done (for a review, see Ref. 33). In particular, the convolution of the $\gamma^* \to q\bar{q}$ diffractive production with the ρ^0 meson wave function gives:

$$R = \frac{\sigma_L}{\sigma_T} \propto \frac{Q^2}{m_{\rho^0}^2}, \tag{20}$$

which has a much too steep dependence with Q^2. A new approach,[33] based on the parton-hadron duality, couples the rise with $Q^2$to the gluon distribution anomalous dimension γ:

$$R = \frac{\sigma_L}{\sigma_\perp} \simeq \frac{Q^2}{M_X^2}(\frac{\gamma}{\gamma+1})^2. \tag{21}$$

Since γ decreases with Q^2, a less steep dependence is obtained that seems to fit

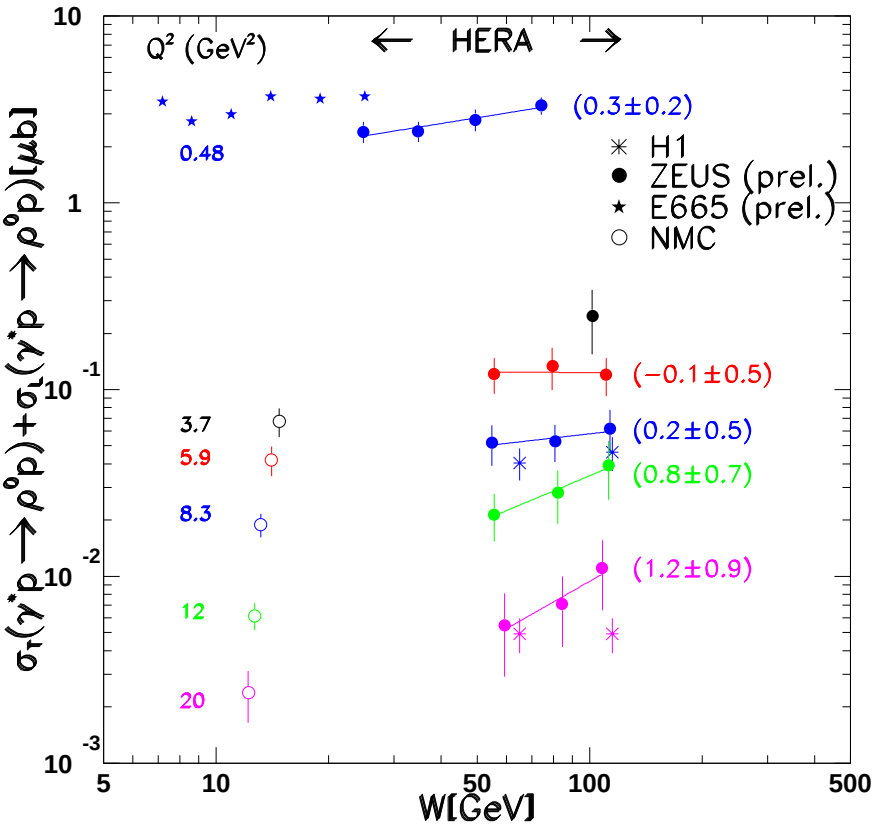

Figure 14: $\gamma p \to \rho^0 p$ cross section as a function of $W_{\gamma p}$for different $< Q^2 >$ values (as indicated in the picture). The lines are the results of fits to the form $\sigma \propto {W_{\gamma p}}^k$; the values of k are shown in parenthesis.

the data quite well. Within the current experimental accuracy, R does not seem to depend on $W_{\gamma p}$.

7.3.2 Determination of $\alpha'_{I\!P}$ at Large Q^2

As we have seen, where Regge theory holds, the value of b should increase with energy according to the "shrinkage" mechanism. The HERA data on photoproduction of ρ^0, ϕ, ω are consistent with this prediction. At high Q^2, there are no pre-HERA measurements of the "shrinkage" mechanism. According to Ref. 56, $\alpha'_{I\!P} \simeq = 0.2$ GeV^{-2} . Therefore, the value of the slope parameter b should increase by ~ 1.5 GeV^{-2} going from low energy, $W_{\gamma p}\sim$ 10 GeV, to the HERA regime, $W_{\gamma p}\sim$ 100 GeV, for all exclusive reactions of the kind $\gamma^* p \to Vp$. On the other

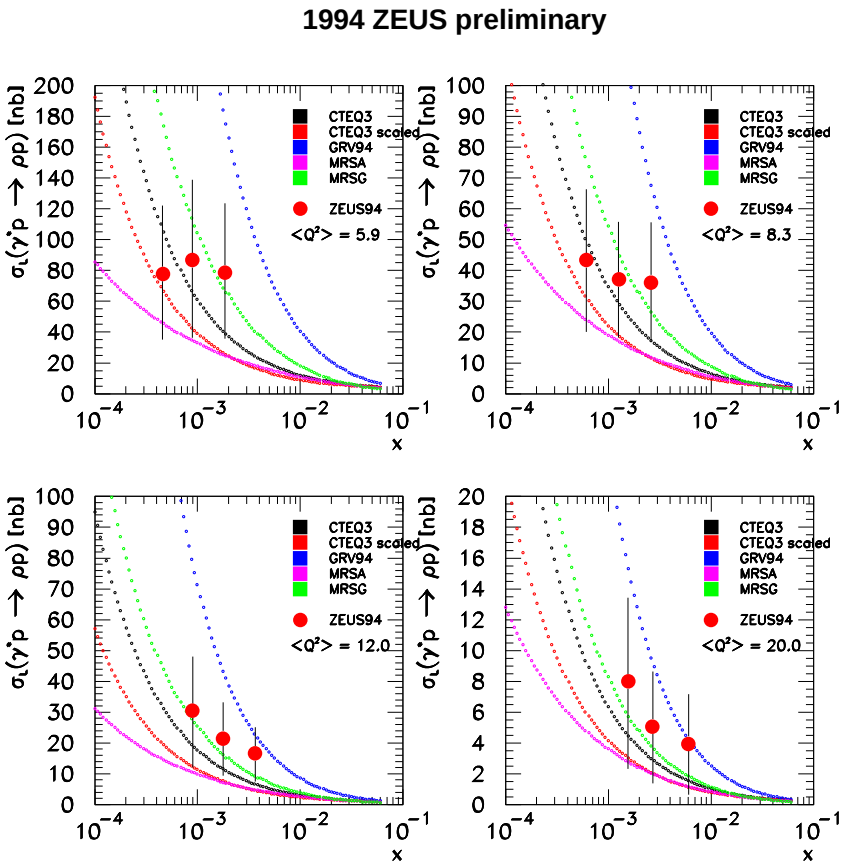

Figure 15: $\gamma p \to \rho^0 p$ cross section as a function of x_{Bj} for different values of $< Q^2 >$. The lines are predictions from a calculation based on pQCD using different gluon distributions.

hand, according to Ref. 57, the value of α'_{IP} is expected to be $\alpha'_{IP} \sim 1/Q^2$ for reactions where the hard QCD regime dominates, leading to a flat behavior of b as a function of W.

Figure 18 shows the b values for the ρ^0 measurements as a function of $W_{\gamma p}$at high Q^2. The experimental data are still dominated by statistical errors, and therefore no meaningful conclusion can be drawn. On the plot, the expected trend of b vs $W_{\gamma p}$is plotted if a value of $\alpha'_{IP} = 0$ or 0.25 is assumed.

According to the SU(4) flavor symmetry, when $M_V^2 \ll Q^2$, the ratio among cross sections for diffractive vector meson production should depend only on the

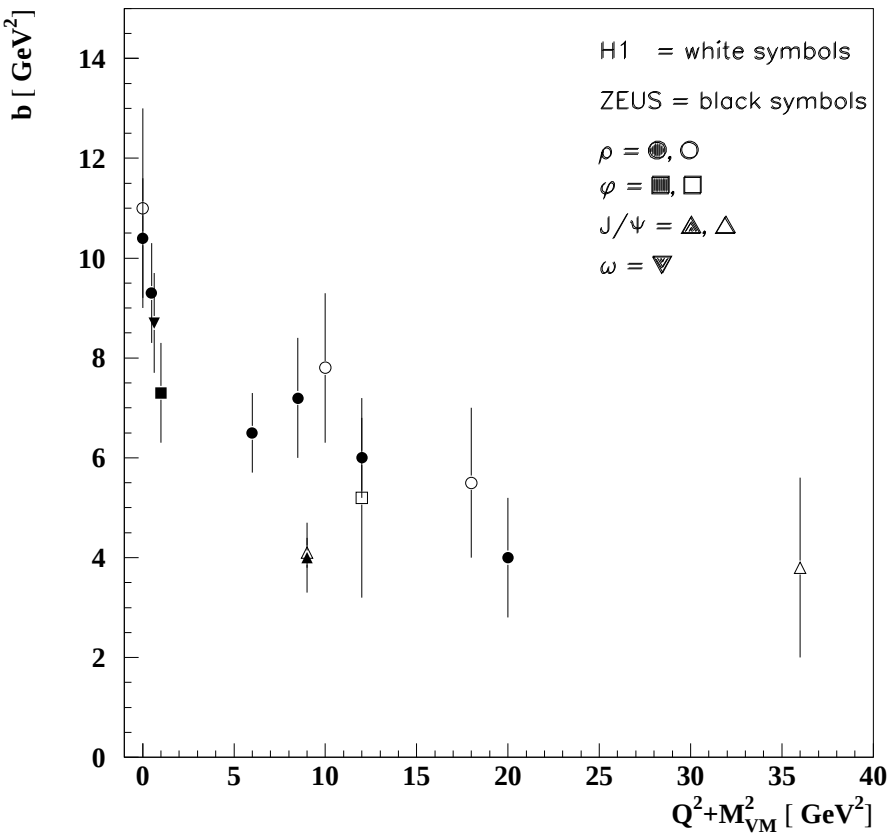

Figure 16: Exponential slope b for vector meson production as a function of $Q^2 + M^2_{VM}$.

meson wavefunction and quark charges[55]:

$$\rho : \omega : \phi : J/\Psi = [\frac{1}{\sqrt{2}}(u\bar{u} + d\bar{d})]^2 : [\frac{1}{\sqrt{2}}(u\bar{u} - d\bar{d})]^2 : [s\bar{s}]^2 : [c\bar{c}]^2 = 9 : 1 : 2 : 8. \tag{22}$$

Besides, QCD dynamics predicts a slow increase of the relative yield of heavy flavor production at small x_{Bj} which modifies the pure SU(4) prediction:

$$\rho : \omega : \phi : J/\Psi = 9 : (1 * 0.8) : (2 * 1.2) : (8 * 3.5). \tag{23}$$

The HERA results are shown in Fig. 19: at $Q^2 \sim 0.$ GeV^2, SU(4) symmetry is badly broken, with a suppression factor $\simeq 4$ for ϕ-mesons and $\simeq 25$ for J/ψ-mesons, while at large Q^2, there is a dramatic increase of both the ϕ *and* J/Ψ cross section compared to ρ^0 meson production. This increase is therefore another indication that the SU(4) symmetry, and therefore perturbative QCD, can be used in these processes at large Q^2.

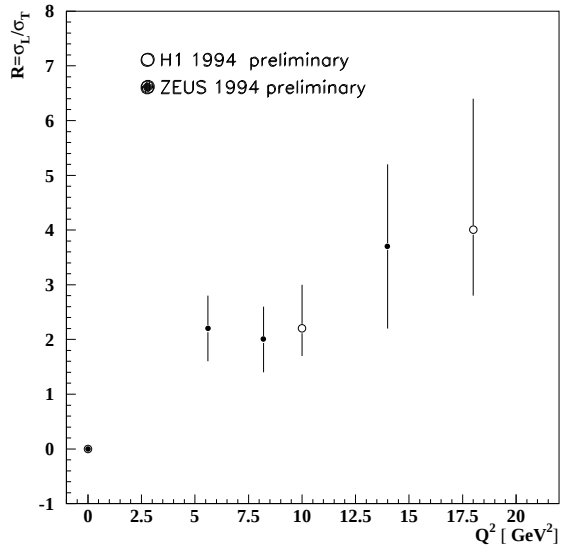

Figure 17: Ratio $R = \sigma_L/\sigma_\perp$ for the reaction $\gamma p \to \rho^0 p$ as a function of the photon virtuality Q^2.

Cross section ratios between excited and ground states for a meson are also very important quantities because they depend on the internal dynamics of the $q\bar{q}$wavefunction and can help to determine it. First preliminary results from the H1 Collaboration,[50,51] in agreement with the expectation of Ref. 55, are:

$$\frac{\sigma^{\rho'}}{\sigma^{\rho}} = 0.36 \ \pm \ 0.07 \ \pm 0.11 \ at \ Q^2 \ = \ 4 - 50 \ GeV^2$$

$$\frac{\sigma^{\Psi(2S)}}{\sigma^{\Psi}} = 0.16 \ \pm \ 0.06 \ at \ Q^2 \ = \ 0 \ GeV^2.$$

8 Photon Diffraction: $\gamma p \to$X Y

Single and double photon diffraction include all Pomeron-mediated reactions of the kind:

$$\gamma p \longrightarrow XY \ ,$$

where X is not a vector meson and Y is either a proton or an excited state. These reactions can be divided into two large groups depending on whether a hard scale is present in the scattering process.

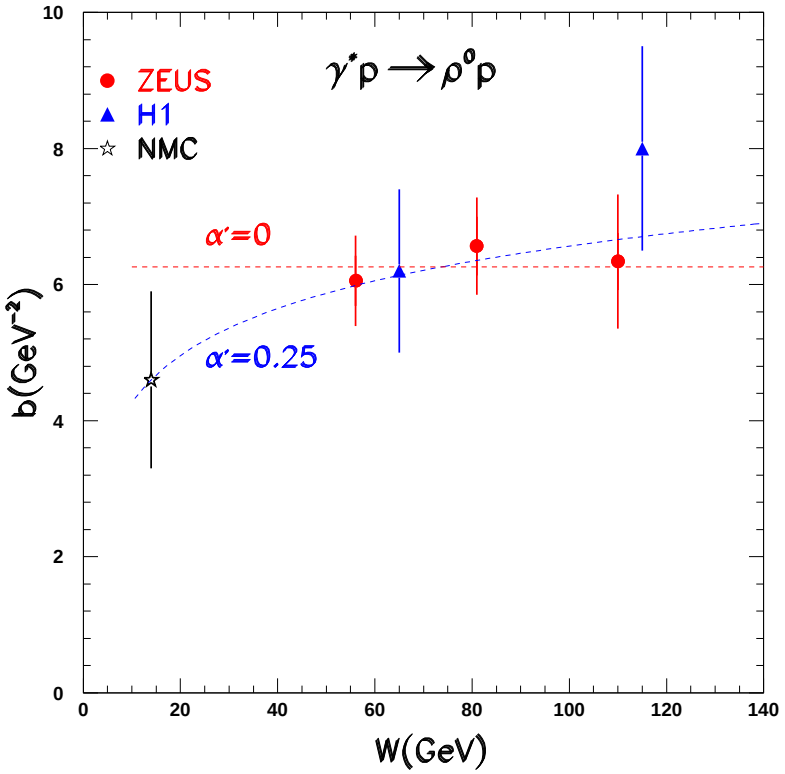

Figure 18: Exponential slope b for the reaction $\gamma p \to \rho^0 p$ as a function of $W_{\gamma p}$. On the plot, the expected trend of b vs $W_{\gamma p}$ is plotted if a value of $\alpha'_{IP} = 0$ or 0.25 is assumed.

8.1 Experimental Signature and Selection Methods for $\gamma p \longrightarrow XY$

As was shown in Sec. 5, diffractive events generally have a rapidity gap and a leading barion in the final state. Several selection methods have been used by both the H1 and ZEUS Collaborations exploiting their own detectors. In the following, the four most significant methods are presented.

8.1.1 Maximum Pseudorapidity η_{max} (ZEUS, H1)

At HERA, following the first papers on the subject,[58,68] a cut on the pseudorapidity of the most forward[¶] energy deposit in an event has been used to separate diffractive from nondiffractive events. This cut selects as diffractive events all those events whose most forward energy deposit has a rapidity less than 1.5,

[¶]As it was said before, in the HERA convention the proton travels along the z-axis in the positive direction.

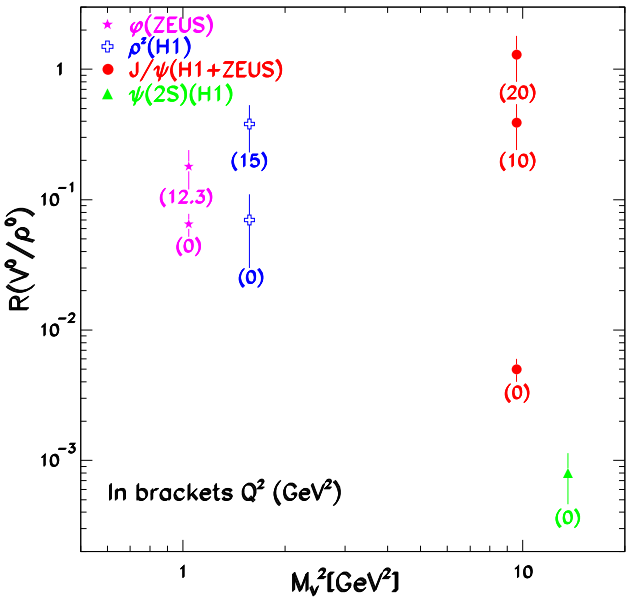

Figure 19: Ratio $R = \sigma^{\gamma p \to V p}/\sigma^{\gamma p \to \rho^0 p}$ as a function of the vector meson mass squared M_V^2 at different values of the photon virtuality Q^2(indicated by the number in parentheses).

equivalent to require a visible rapidity gap of at least 2.9 units in the forward direction (ZEUS case). This cut, however, puts strong limitations on the type of events that are selected since it reduces the pseudorapidity interval available for the fragmentation of the system M_X to $\Delta\eta \simeq 4.5$–5.5. Since a system with mass M_X covers a pseudorapidity interval $\Delta\eta \simeq ln(\frac{M_X^2}{m_p^2})$ with m_p the proton mass, only masses up to $M_X \sim 10$–15 GeV are therefore selected.

8.1.2 Largest Rapidity Gap (H1)

For each event, the largest rapidity gap is identified, Fig. 20. This gap defines two systems, X and Y with masses M_X and M_Y. If:

(a) $x_{I\!P} = \frac{M_X^2+Q^2}{W_{\gamma p}^2+Q^2} < 0.05$

(b) $M_Y < 1.6\ GeV$,

the event is accepted in the diffractive sample. This selection is based on the H1 detector ability of measuring hadronic activity up to $\eta \sim 3.4 \Rightarrow x_{I\!P} < 0.05$ and vetoing activity in the region $3.4 < \eta < 7.5 \Rightarrow M_Y < 1.6$ GeV.

The requirement (a) ensures that only a small fraction of the initial proton longitudinal momentum is present in the detector, while (b) forces the existence of a rapidity gap in the final state. It is important to notice that this selection

criterium does not make any assumption on the nature of the interaction but defines a cross section for all events that are selected by (a) and (b).

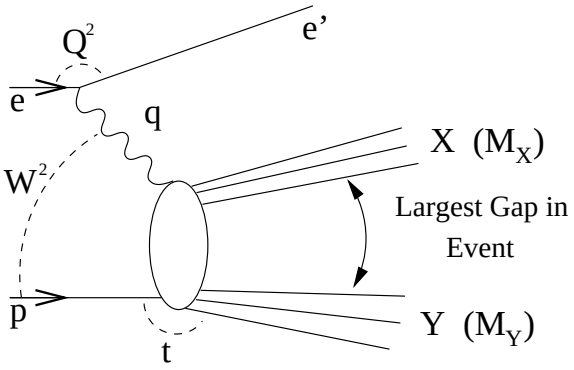

Figure 20: Schematic illustration of the selection method used to define a diffractive cross section by the H1 Collaboration.

8.1.3 Leading Proton Measurement (ZEUS_LPS)

The cleanest way to identify diffractive events is to tag a scattered proton with a very high fraction x_L of the initial proton momentum. From the leading proton momentum, both t and the hadronic mass M_X can be computed:

$$t \simeq -\frac{p_t^2}{x_L} \tag{24}$$

$$M_X^2 = W_{\gamma p}^2 \cdot (1 - x_L). \tag{25}$$

Figure 21 shows the fraction of DIS events with a leading proton as a function of x_L for $5 < Q^2 < 20$ GeV^2, $45 < W_{\gamma p} < 225$ GeV, and $(1 - x_L)^2/x_L < |t| < 0.5$ GeV^2. Comparing this figure with Fig. 7, two different components can be easily identified: the diffractive peak due to $\mathbb{P}$ exchange at $x_L \sim 1$ and the continuum due to double dissociation, reggeon exchange, and nondiffractive DIS scattering rising below $x_L \sim 0.9$. Just below $x_L \sim 1$, the distinction between diffractive and nondiffractive events becomes unclear. From a fit to the x_L spectrum in pp scattering,[60] the value $x_L \sim 0.9$ has been used to identify the point where the Pomeron and non-Pomeron contributions are roughly of the same magnitude. The ZEUS Collaboration, in order to select a very pure diffractive sample, decided to use only protons with $x_L > 0.97$, well within the diffractive peak. Unfortunately, due to the limited LPS acceptance, the number of events with a tagged leading proton is small. Note that the LPS acceptance, at x_L >0.95, starts at $t \sim 0.07$ GeV^2.

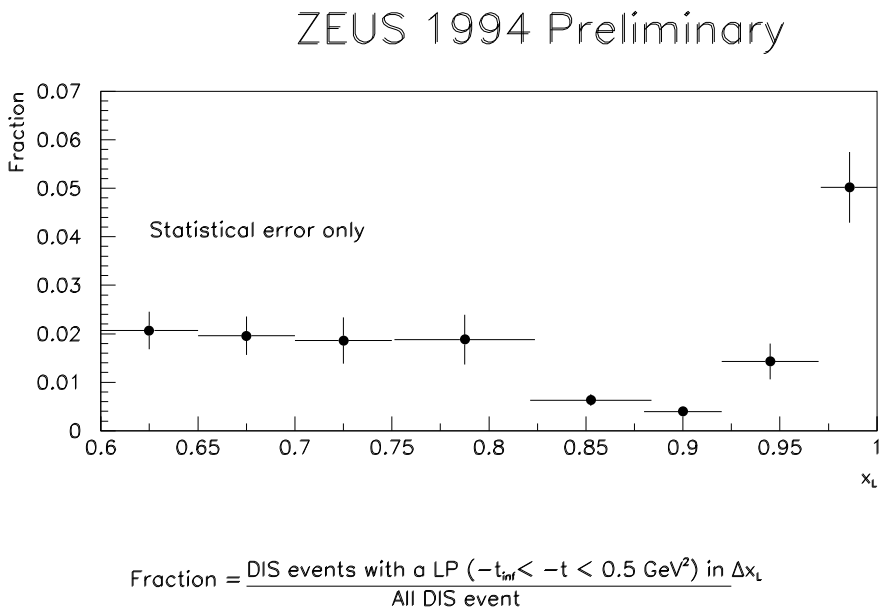

Figure 21: Fraction of DIS events with a leading proton as a function of x_L.

8.1.4 Ln(M_X) Distribution (ZEUS_MX)

This method[59] of separating the diffractive and nondiffractive contributions is based on their very different M_X^2 distributions. Nondiffractive events, assuming uncorrelated particle emission, have an exponential fall-off of the $\ln M_X^2$ distribution:

$$\frac{d\mathcal{N}^{nondiff}}{d\ln M_X^2} = c\ \exp(b \ln M_X^2) \quad , \tag{26}$$

while diffractive events have a constant value in the $\ln M_X^2$ distribution:

$$\frac{dN}{dM_X^2} \sim \frac{1}{M_X^2} \Longrightarrow \frac{dN}{d\ln M_X^2} \ = \ const. \tag{27}$$

The diffractive sample is therefore defined as the excess contribution in the $\ln M_X^2$ distribution above the exponential fall-off of the nondiffractive peak. In bins of $W_{\gamma p}$, Q^2, and M_X , a fit in the form:

$$\frac{dN}{d\ln M_X^2} = D + c\ \exp(b \ln M_X^2) \tag{28}$$

is performed allowing the evaluation of the diffractive component. An example of the $\ln M_X^2$ distribution is given in Fig. 22.

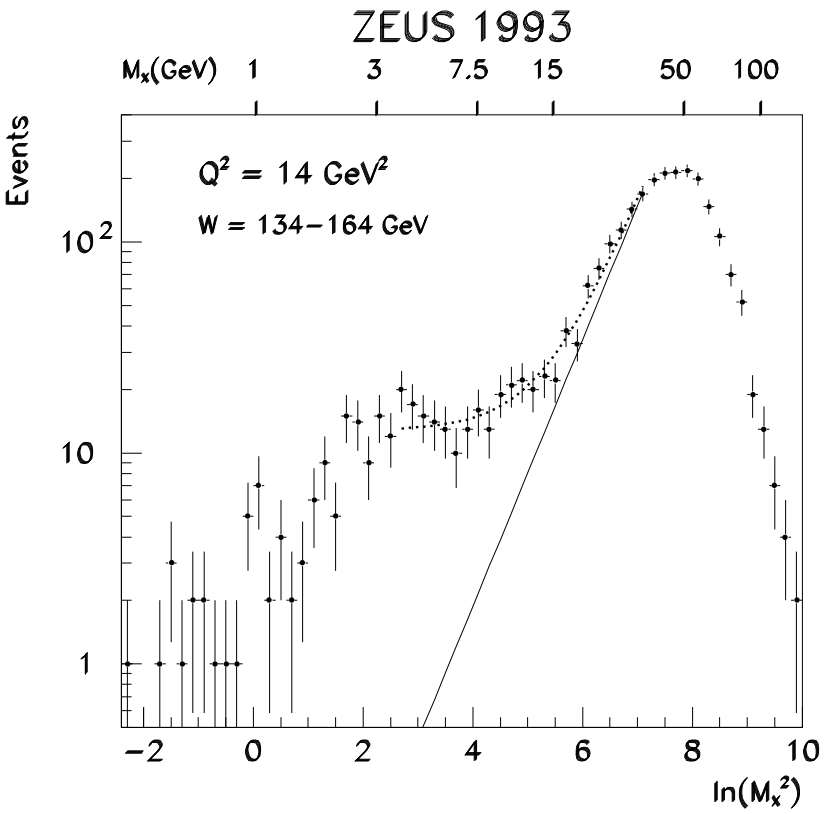

Figure 22: ln M_X^2 distributions for $\gamma^* p$ scattering. Diffractive events are identified as the excess contribution above the exponential fall-off of the nondiffractive peak.

8.2 Determination of $\alpha_{I\!P}$ and Test of Factorization

The assumption of factorization implies that the Pomeron structure is independent of the process of emission and that the Pomeron flux is the same in all diffractive processes. Its dependence on $\alpha_{I\!P}$ is given by:

$$f_{I\!P/p}(x_{I\!P}) \propto (\frac{1}{x_{I\!P}})^a \quad , \tag{29}$$

with $a = 2\alpha_{I\!P}(0) - 1$. If factorization holds, the same value of $\alpha_{I\!P}(0) \simeq 1.08$ measured in many hadronic reactions should also control the Pomeron flux at HERA.

8.2.1 Determination of $\alpha_{I\!P}$ at $Q^2 \simeq$ 0 GeV^2

The value of $\alpha_{I\!P}(0)$, as shown in Sec. 2, can be measured directly from the behavior of $\sigma_{tot}^{\gamma p}(W)$ as a function of the center-of-mass energy $W_{\gamma p}$. Results from both the H1 and ZEUS Collaborations are consistent with a value of $\alpha_{I\!P}(0) \simeq 1.08$ (see Sec. 2).

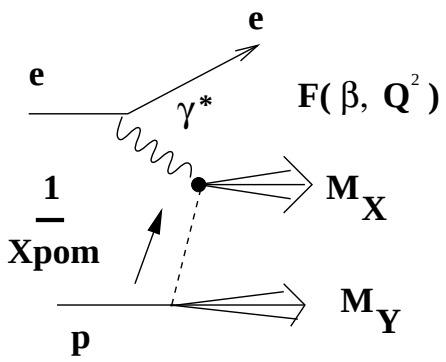

Figure 23: Diffractive ep scattering according to factorization: the flux of the Pomeron and the Pomeron structure function are universal quantities that can be determined separately.

Collaboration	M_X Interval [GeV]	$\alpha_{IP}(0)$
ZEUS	$8 < M_X < 24$	$1.14 \pm 0.04\,(stat) \pm 0.08\,(syst)$
H1	$3 < M_X < 24$	$1.11 \pm 0.02\,(stat) \pm 0.07\,(syst)$

Table 4: $\alpha_{IP}(0)$ values in diffractive photoproduction as determined by the H1 and ZEUS Collaborations from a fit to $\frac{d^2\sigma}{d|t|dM_X^2}$.

A second method to determine $\alpha_{IP}(0)$ is based on the behavior of the differential cross section $\frac{d^2\sigma}{d|t|dM_X^2}$ as calculated in the Regge formalism for the triple Pomeron diagram:

$$\frac{d^2\sigma}{d|t|dM_X^2} \propto (\frac{1}{M_X^2})^{\alpha_{IP}(0)} \cdot e^{(b_o + 2\alpha'_{IP} ln(\frac{W_{\gamma p}^2}{M_X^2})) \cdot |t|} \quad . \tag{30}$$

In Table 4, the results from the H1 (Ref. 61) and ZEUS 62 Collaborations are presented. Both results suggest a value for $\alpha_{IP}(0)$ consistent with Regge phenomenology as already indicated by $\sigma_{tot}^{\gamma p}(W)$ and support the hypothesis that the same "soft Pomeron" used to describe the high-energy behavior of hadron-hadron scattering is also responsible for diffractive photoproduction at HERA.

8.2.2 Determination of $\alpha_{I\!P}$ at Large Q^2

At large Q^2, by analogy with standard deep inelastic scattering, the differential cross section for deep inelastic diffractive scattering can be written as:

$$\frac{d^4\sigma_{diff}}{dQ^2 d\beta dx_{I\!P} dt} = \frac{2\pi\alpha^2}{\beta Q^4}\,(1+(1-y)^2)\,F_2^{D(4)}(Q^2,\beta,x_{I\!P},t). \qquad (31)$$

Using now the assumption that factorization is valid, the t and $x_{I\!P}$ dependence can be separated from the dependence on β and Q^2:

$$F_2^{D(4)}(Q^2,\beta,x_{I\!P},t) = f(x_{I\!P},t)\cdot F_2^{D(2)}(Q^2,\beta).$$

Integrating the Pomeron flux over t and writing the dependence on $x_{I\!P}$ explicitly, $F_2^{D(4)}(Q^2,\beta,x_{I\!P},t)$ becomes:

$$F_2^{D(4)}(Q^2,\beta,x_{I\!P},t) \;\;\Rightarrow\;\; (\frac{1}{x_{I\!P}})^a \cdot F_2^{I\!P}(Q^2,\beta). \qquad (32)$$

Following Eqs. 31 and 32, the determination of the DIS diffractive cross section in $x_{I\!P}$bins provides a method to measure $\alpha_{I\!P}$ as a function of $Q^2$and β and to test whether factorization holds.

H1 determination of $\alpha_{I\!P}$

Figure 25 shows the quantity $x_{I\!P}\cdot F_2^{D(2)}(\beta,Q^2)$ for different $Q^2$and β bins as a function of $x_{I\!P}$. The data[64] were fitted with the function:

$$F_2^{D(3)} = (\frac{1}{x_{I\!P}})^a \cdot A(\beta,Q^2)$$

in each β *or* Q^2 interval. The points clearly show a change in slope going from low to high values of β while no dependence is seen with Q^2, Fig. 24. This analysis, therefore, shows that there is a change in the value of n as a function of $x_{I\!P}$and β. This experimental factorization breaking, however, does not uniquely indicate a change in the Pomeron flux, but it might also be explained in terms of a presence in the data of a "non-Pomeron" component. If a fit using a meson and a Pomeron component is performed, Fig. 25,

$$F_2^{D(3)} = F_2^{I\!P}(\beta,Q^2)\cdot {x_{I\!P}}^{-a} + C_M\cdot F_2^M(\beta,Q^2)\cdot {x_{I\!P}}^{-n_2},$$

then a single value for "a" gives a good description of the data (preliminary results):

$$a \;=\; 1.29 \;\pm\; 0.03\,(stat) \;\pm\; 0.06(syst) \;\pm\; 0.03\,(model)$$

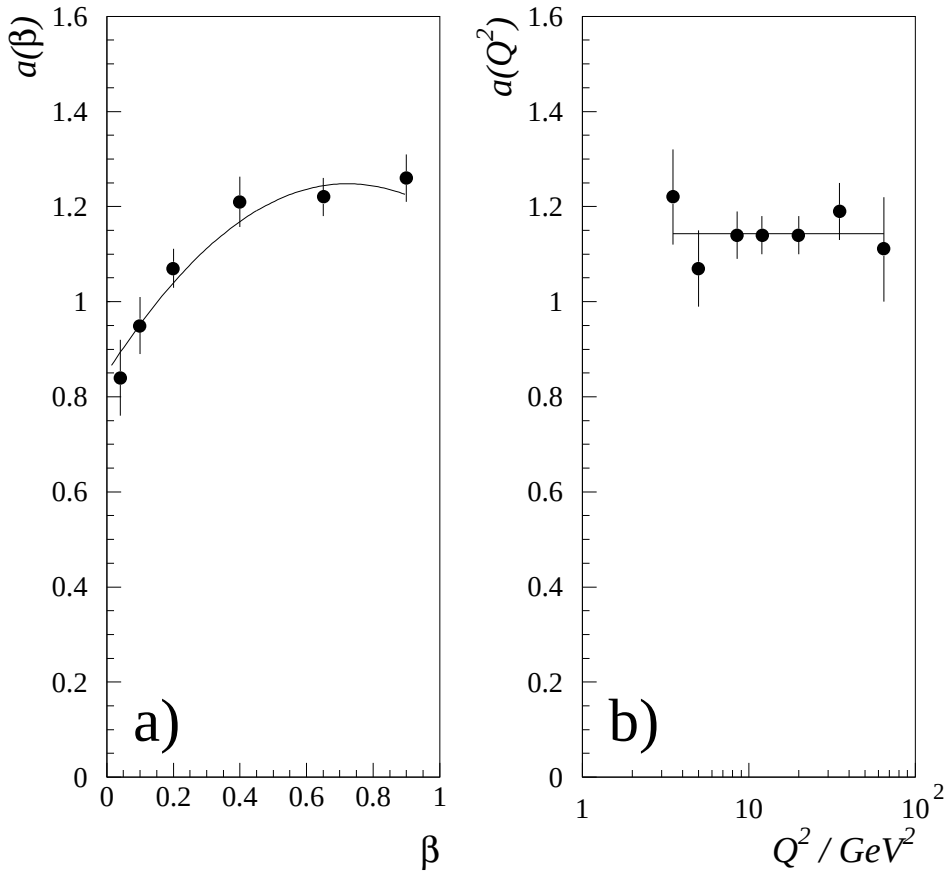

Figure 24: Results for the value of a when $F_2^{D(2)}(\beta, Q^2)$ is fitted to the form $(\frac{1}{x_{I\!P}})^{a(\beta)}$. Statistical and systematic errors are added in quadrature.

$$n_2 \;=\; 0.3 \;\pm\; 0.3\,(stat) \;\pm\; 0.6\,(syst) \;\pm\; 0.2\,(model)$$

with $\chi^2/ndf = 170/156$. The value obtained for n_2 is consistent with what is expected from meson exchange. From "a", a value for $\alpha_{I\!P}$ averaged over the unmeasured t distribution, $\overline{\alpha_{I\!P}}$, can be obtained, $\overline{\alpha_{I\!P}} = \frac{a+1}{2}$:

$$\overline{\alpha_{I\!P}}^{H1} = 1.15 \pm 0.02\,(stat) \;\pm 0.04\,(syst).$$

To check consistency between results obtained with this method and a previous H1 analysis,[68] the measurement of $\alpha_{I\!P}$ using a single component has also been performed over the same kinematical range used in Ref. 68, obtaining a result that is compatible within statistical errors with the old one.

H1 Preliminary 1994

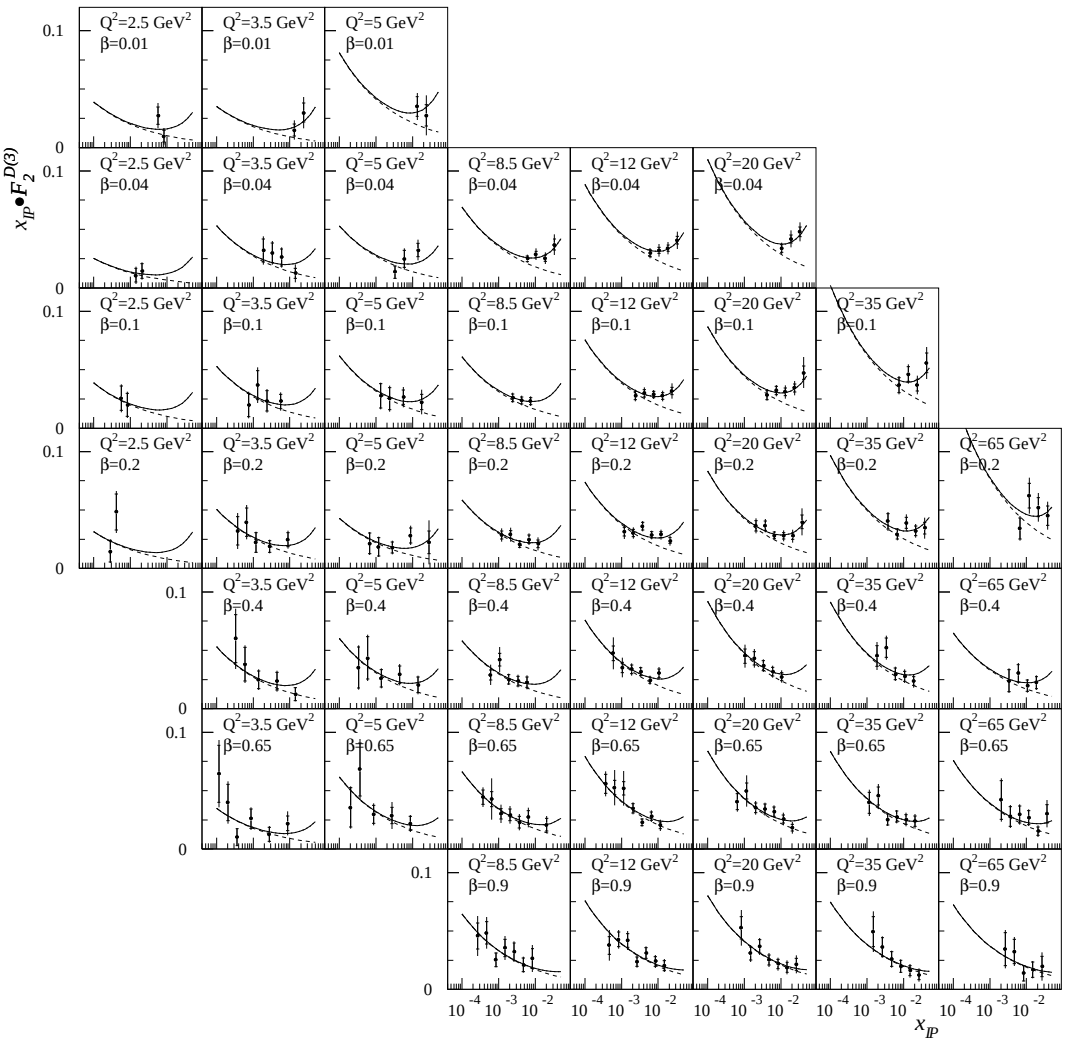

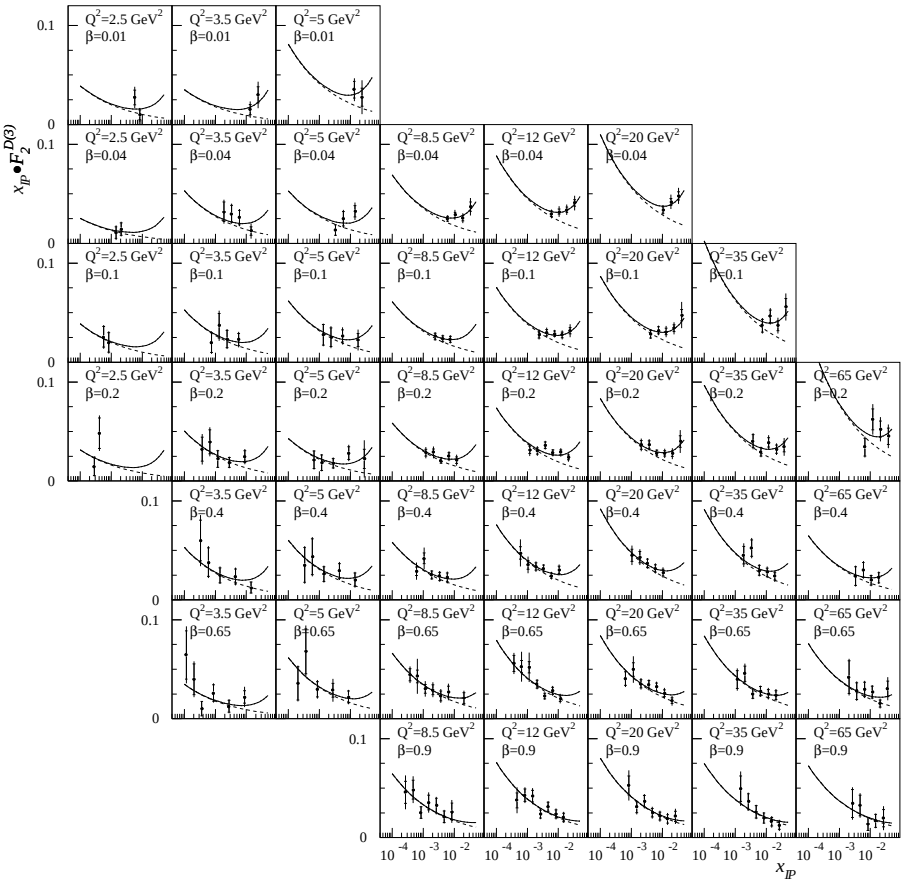

Figure 25: $x_{IP} \cdot F_2^{D(2)}(\beta, Q^2)$ together with a fit in which a Pomeron component with a trajectory α_{IP} contributes together with a meson component with trajectory α_M. On each plot, the bottom line shows the contribution from the Pomeron component while the top line shows the sum of the two components.

ZEUS_LPS determination of α_{IP}

The diffractive structure function $F_2^{D(3)}(\beta, Q^2, x_{IP})$ was determined using LPS tagged events[65] in the range $4 < Q^2 < 30$ GeV^2, $0.006 < \beta < 0.5$, $< Q^2 >= 12$ GeV^2, $4 \cdot 10^{-4} < x_{IP} < 3 \cdot 10^{-2}$, and $0.07 < |t| < 0.36$ GeV^2, extending the range to lower β and higher x_{IP} compared to previous ZEUS measurements (Fig. 26). The results are consistent with factorizable x_{IP} dependence in all β bins. Fitting the highest three β bins with the same exponent gives a= 1.28 $\pm$ 0.07 (stat.) $\pm$ 0.15 (syst.), and therefore:

$$\overline{\alpha_{IP}}^{LPS} \; = \; 1.14 \; \pm \; 0.04\,(stat.) \; \pm \; 0.08\,(syst) \quad .$$

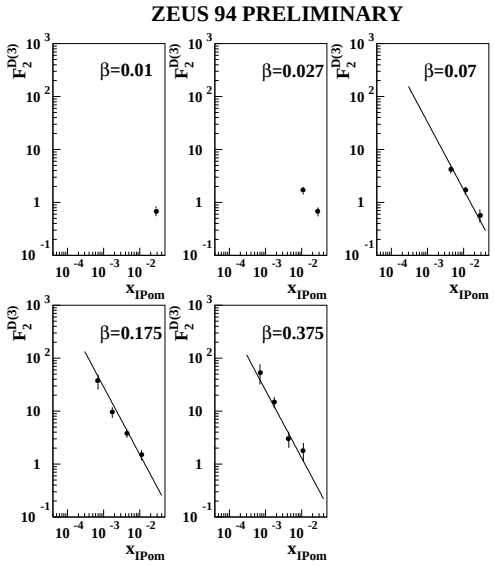

Figure 26: The structure function $F_2^{D(2)}(\beta, Q^2)$ plotted vs $x_{I\!P}$ in bins of β at $< Q^2 >= 12\,\mathrm{GeV}^2$. The errors are statistical only. The solid line corresponds to the fit described in the text.

ZEUS_Mx determination of $\alpha_{I\!P}$

The determination of $\alpha_{I\!P}$ can also be achieved by fitting the energy dependence of the cross section in bins of M_X (Ref. 59). In a Regge-type description,[66,67] the $W_{\gamma p}$dependence of the diffractive cross section is of the form

$$\frac{d\sigma_{diff}^{\gamma^* p \to XN}(M_X\ , W_{\gamma p}, Q^2, t)}{dt dM_X} \propto ({W_{\gamma p}}^2)^{2\alpha_{I\!P}(0)-2}\ \cdot\ e^{-|t|(b_0+2\alpha'_{I\!P}\ln(W_{\gamma p}^2/(M_X^2+Q^2)))} \quad ,(33)$$

where $\alpha_{I\!P}(t) = \alpha_{I\!P}(0) + \alpha'_{I\!P}t$ is the Pomeron trajectory and b_0 and $\alpha'_{I\!P}$ are parameters. The cross sections in each $(M_X\ , Q^2)$ interval is fitted to the form

$$\frac{d\sigma_{diff}^{\gamma^* p \to XN}(M_X\ , W_{\gamma p}, Q^2)}{dM_X} \propto ({W_{\gamma p}}^2)^{(2\overline{\alpha_{I\!P}}-2)} \quad , \qquad (34)$$

allowing a determination of $\overline{\alpha_{I\!P}}$. Howewer, the result obtained with this method is currently under further investigation and is shown only for completeness‖:

‖In the preliminary analysis of the ZEUS '94 data on the diffractive DIS cross sections, a technical mistake has been found in the generation of the Monte Carlo data used for the acceptance correction and resolution unfolding. This mistake led to the mishandling of QED radiative corrections. Its effect is to change the cross sections by typically one systematic error. The ZEUS Collaboration thus has retracted their 1994 preliminary results until further analysis is completed and the effect on the above value of $\overline{\alpha_{I\!P}}^{M_X}$ is currently under study.

$$\overline{\alpha_{I\!P}}^{M_X} \quad = \quad 1.23 \pm 0.02(stat) \pm 0.04(syst).$$

8.2.3 Comparison of the Results

In order to compare results obtained at $Q^2 \sim 0$ GeV with results obtained at large Q^2, the influence on the result of the unknown value of $\alpha'_{I\!P}$ in photon diffraction at large Q^2needs to be evaluated. Note that the value of $\alpha'_{I\!P}$ in photon diffraction at large Q^2does not have to be the same one measured in vector meson production in the presence of a hard scale. Let's consider, as an example, the $\ln M_X$ analysis. Integrating over t Eq. 33, the expression for the cross section is:

$$\frac{d\sigma_{diff}^{\gamma^* p \rightarrow XN}(M_X\ , W_{\gamma p}, Q^2)}{dM_X} \propto ({W_{\gamma p}}^2)^{2\alpha_{I\!P}(0)-2} \cdot \frac{1}{b_0 + 2\alpha'_{I\!P} \ln({W_{\gamma p}}^2/(M_X^2+Q^2))}$$
$$e^{-|t|(b_0+2\alpha'_{I\!P} \ln(W_{\gamma p}^2/(M_X^2+Q^2)))} \Big|_{|t_{max}|}^{|t_{min}|}. \qquad (35)$$

If $\alpha'_{I\!P} \sim 0.$ GeV^{-2}, then Eq. 35 simplifies to

$$\frac{d\sigma_{diff}^{\gamma^* p \rightarrow XN}(M_X\ , W_{\gamma p}, Q^2)}{dM_X} \propto ({W_{\gamma p}}^2)^{2\alpha_{I\!P}(0)-2},$$

and comparing this expression with Eq. 34, we obtain $\overline{\alpha_{I\!P}} = \alpha_{I\!P}(0)$. On the other hand, if $\alpha'_{I\!P} > 0.$ GeV^{-2}, then two effects change the slope of the $W_{\gamma p}$dependence:

(1) The denominator of Eq. 35 is a slowly rising function of $W_{\gamma p}$and therefore causes $\overline{\alpha_{I\!P}}$ to be smaller than $\alpha_{I\!P}$. This effect has been estimated, for $\alpha'_{I\!P} =$ 0.25 GeV^{-2}, to be 0.025–0.03.

(2) If the t range is limited, the last term of Eq. 35 is a decreasing function of $W_{\gamma p}$, causing $\overline{\alpha_{I\!P}}$ to be smaller than $\alpha_{I\!P}$. For the ZEUS_LPS analysis, where $|t_{min}| = 0.07\ GeV^2$, a value of $\alpha'_{I\!P} = 0.25$ GeV^{-2} reduces the measured $\overline{\alpha_{I\!P}}$ value by ~ 0.02.

In Fig. 27, the compilation of $\alpha_{I\!P}$ values obtained at HERA is shown assuming, for the measurement at large Q^2, (a) $\alpha'_{I\!P} = 0$ GeV^{-2}; or (b) $\alpha'_{I\!P} = 0.25$ GeV^{-2} . The solid line is the statistical error while the dotted line is the systematic error. The values indicated as H1 93 (η_{max}) (Ref. 68) and ZEUS 93 (η_{max}) (Ref. 69) are the first measurement obtained by each experiment, and they were obtained using the selection cut $\eta_{max} < 1.8$ for H1 and $\eta_{max} < 1.5$ for ZEUS.

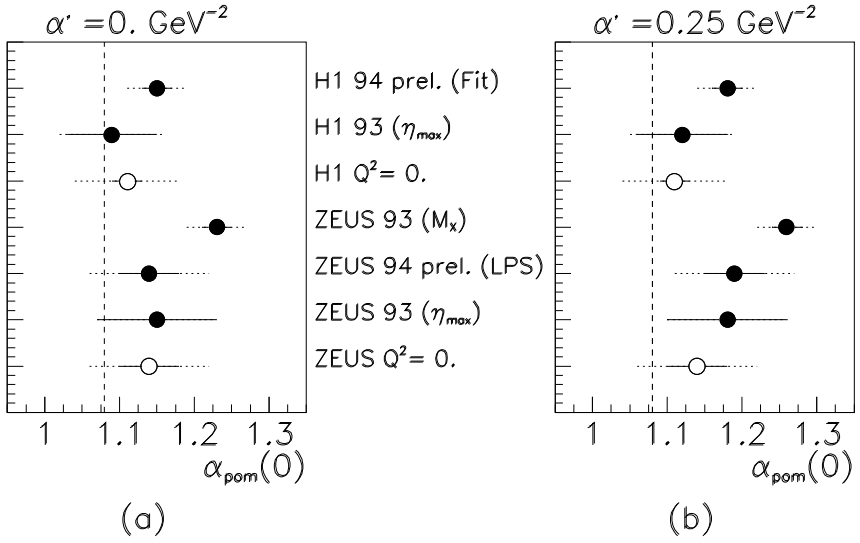

Figure 27: Compilation of $\alpha_{IP}(0)$ values obtained at HERA, assuming, for the measurement at large Q^2, (a) $\alpha'_{IP} = 0.0$ GeV^{-2}; or (b) $\alpha'_{IP} = 0.25$ GeV^{-2}. Empty dots are values obtained at Q^2= 0.0 GeV^2, full dots at high Q^2. The dashed vertical line is the value $\alpha_{IP}(0) = 1.08$. The solid line is the statistical error while the dotted line is the systematic error.

It is possible that the difference in value between ${\alpha_{IP}}^{Q^2=0}(0)$ and ${\alpha_{IP}}^{Q^2>0}(0)$ is a signal for the presence of a small "hard" Pomeron component in the diffractive sample at high Q^2. How to measure it, its magnitude, and how to enhance it choosing particular final states (for example, see Refs. 70,71) is currently under intense theoretical investigation. Note also that the above comparison is done among measurements performed on different t and x_{IP} ranges.

8.3 Measurement of the Slope Parameter b in Diffractive DIS

Using the ZEUS leading proton spectrometer, the t distribution of diffractive DIS was measured directly for the first time at HERA.[65] The measurement of t has been performed in the kinematic range: $x_L > 0.97$, $4 < Q^2 < 30\ GeV^2$, $< Q^2 >= 12 GeV^2$, $70 < W_{\gamma p} < 210$ GeV, $0.07 < |t| < 0.36$ GeV^2. Assuming an exponential behavior $\frac{d\sigma}{dt} \propto e^{-b|t|}$, b is measured to be:

$$b = 5.9 \pm 1.3\ (stat.)\ ^{+1.1}_{-0.7}\ (syst) GeV^{-2}.$$

The measured t distribution is shown in Fig. 28. The value of b is similar to the values obtained in single diffraction in pp interactions.

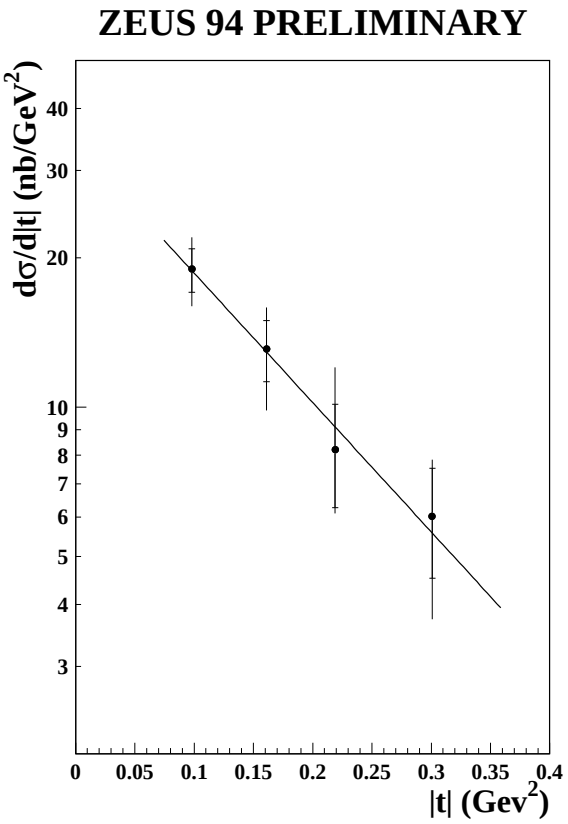

Figure 28: Differential cross section $\frac{d\sigma}{dt}$ for diffractive DIS events with a leading proton detected in the LPS. The error bars represent the statistical and systematic errors added in quadrature, and the line shows the result of the exponential fit.

8.4 Partonic Structure of Diffractive Exchange

8.4.1 QCD Fit to the Diffractive Structure Function

The H1 Collaboration[64] performed a QCD analysis of the diffractive structure function $F_2^{D(3)}(Q^2, \beta, x_{I\!P})$. The analysis is performed integrating $F_2^{D(3)}(Q^2, \beta, x_{I\!P})$ over the measured $x_{I\!P}$ range, and the result interpreted as the deep inelastic structure of the exchanged object averaged over t and $x_{I\!P}$:

$$\tilde{F}_2^{I\!P}(Q^2, \beta) = \int_{x_{I\!P\,min}}^{x_{I\!P\,max}} (\frac{1}{x_{I\!P}})^n \cdot F_2^{I\!P}(Q^2, \beta) \cdot dx_{I\!P}.$$

The QCD analysis is performed fitting the data using a flavor singlet quark and gluon distribution ($u + \bar{u} + d + \bar{d} + s + \bar{s} + gluon$) at a starting scale $Q_0^2 = 2.5\, GeV^2$ and then evolving the system according to the DGLAP[72] evolution equation. The results are shown in Fig. 29. The most striking feature in the data is that a rise with $\ln Q^2$persists to values of β far in excess of the point ($x_{Bj} \simeq 0.15$) at which the structure of the proton is dominated by quarks rather than by gluons, suggesting a strong gluonic component in the structure of the diffractive exchange. The QCD fit supports this interpretation: the analysis has also been done considering only quarks at the starting scale Q_0^2 and a much wors χ^2 value has been obtained. The parton distributions obtained from the fit are shown in Fig. 30. At Q^2= 5 GeV^2, a "leading" gluon behavior is observed, in which the exchange is dominated by gluons carrying a very large fraction of the longitudinal momentum.

8.4.2 Jet Structure

The question of the constituent content of the Pomeron can also be addressed via measurements of diffractively produced jets, both in photoproduction[73,74] and DIS.[75] The ZEUS Collaboration studied the diffractive dijet cross section:

$$\gamma p \longrightarrow jet + jet + X + p$$

and compared its magnitude and shape with different model predictions based on a factorizable model of Pomeron. To ensure diffractive production, a gap in the most forward part of the detector of at least 2.9 units was required. The following Pomeron fractional momentum densities were used in the MC:
Super-hard gluon: $\beta f_{g/I\!P}(\beta) = \frac{0.1}{(1-\beta)^{0.9}}$
Hard gluon: $\beta f_{g/I\!P}(\beta) = 6\beta(1-\beta)$ $, < \beta >= 1/2$
Hard-quark (2 flavors): $\beta f_{q/I\!P}(\beta) = \frac{6}{4}\beta(1-\beta)$.
The measured distribution, Fig. 31, is compatible with a Pomeron containing a hard-gluon density. The thick error bars represent the statistical errors of the data, and the thin error bars show the statistical error added in quadrature with the systematic non-associated with the jet energy scale. Comparison with POMPYT[76] MC calculations for a gluonic (quarkonic) Pomeron are shown, including both direct and resolved contributions and different choices of the parton density. From top to bottom, the curves correspond to super-hard gluon (dashed-dotted), hard gluon, hard quark, and soft gluon. The nondiffractive contribution modelled by PYTHIA[77] is shown as a dashed line.

8.5 $\sigma_{dif}/\sigma_{tot}$ as a function of Q^2

Figure 32 shows the ratio between the diffractive and total cross section as a function of Q^2. At $Q^2 \sim 0$ GeV^2, the diffractive part of the cross section is $36 \pm 8\%$ ($42 \pm 8\%$) according to the ZEUS (H1) Collaboration of which $23 \pm 6\%$ (32 ± 4 %) is photon diffraction and 13±5 % (10±3%) is vector meson production. This last component has been measured to fall at least like $d\sigma/dQ^2 \sim 1/(m_{VM}^2 + Q^2)^2$ and therefore becomes negligible as Q^2increases. Photon diffraction seems to decrease going from $Q^2 = 0$ to 10 GeV^2, while it stays flat as a function of Q^2at large Q^2, indicating that diffraction is a leading twist mechanism. It will be very interesting to have more accurate data to see if this decrease, assuming that it is actually confirmed, happens at the same Q^2values where pQCD starts to be applicable, indicating a change in the nature of the γp diffractive interaction.

9 Central Rapidity Gaps

In high-energy hadronic collisions, the dominant mechanism for jet production is a hard scatter between partons in the incoming hadrons via a quark or gluon propagator. Such jets are said to be "color connected," and this leads to the production of particles throughout the rapidity region between the jets. However, if the hard scattering were mediated by the exchange of a color singlet propagator in the t-channel, each jet would be color connected only to the beam remnant closest in rapidity, and the rapidity region between the jets would contain few final-state particles,[78] Fig. 33(a and b).

D0 (Ref. 79) and CDF (Ref. 80) have reported the results of searches at $\sqrt{s} = 1.8$ TeV for dijet events in $p\bar{p}$ collisions containing a rapidity gap between the two highest transverse energy (E_T^{jet}) jets. Both collaborations see an excess of gap events over the expectations from color exchange processes. D0 reports an excess of $0.0107 \pm 0.0010(stat.)^{+0.0025}_{-0.0013}(syst.)$, whereas CDF measures the fraction to be 0.0086 ± 0.0012.

At HERA, an equivalent mechanism is possible, with the hadronic fluctuation of the photon acting as one of the hadrons. In order to quantify the rapidity gap events, a gap fraction, $f(\Delta\eta)$, is defined as the ratio of the number of dijet events which have a rapidity gap of width $\Delta\eta$ between the jets to the total number of dijet events. As explained above, for color nonsinglet exchange, the gap fraction is

expected to fall exponentially with increasing $\Delta\eta$, while for color singlet exchange, the gap fraction is not expected to depend strongly upon $\Delta\eta$ (Ref. 15,81). The situation is illustrated in Fig. 33(d).

The results[82] are shown in Fig. 34. Both the comparison with the default PYTHIA non singlet prediction and the fit to an exponential form give an excess of about 0.07 in the gap fraction over the expectation from color non singlet exchange. This excess can be interpreted as evidence of hard diffraction: a simple two-gluon model for Pomeron exchange gives $\hat{f}(\Delta\eta) \sim 0.1$[15] thus showing that Pomeron exchange could account for the data.

The magnitude of the squared four-momentum transfer across the rapidity gap as calculated from the jets is large ($|t| \geq (E_T^{jet})^2$). Thus, the color singlet exchange is unambiguously "hard."

10 Conclusions

Diffraction at HERA has provided many measurements in both the soft and perturbative domains.

- The rise of the total γp cross section has been measured to be weak, consistent with the exchange of the same "soft" Pomeron responsible for the rise with energy of hadronic reactions.
- Diffractive photoproduction is also governed by soft Pomeron exchange: a value of $\alpha_{I\!P}(0) \simeq 1.11 - 1.14$ has been measured from the mass spectrum of the dissociated photon in the triple Pomeron regime.
- Elastic vector meson production at HERA shows a clear distinction between two classes of processes. A first group of results, photoproduction of light vector mesons ($\gamma p \to Vp$, $V = \rho^0$, ϕ ω), exhibits the characteristic features of diffraction, as described by Regge theory: a weak energy dependence of the cross section and a value of the t slope parameter b as observed in hadronic diffractive reactions. They are therefore explained in terms of the same Pomeron that controls the total cross section. A second group, which includes photoproduction of J/ψ and light vector meson production at high Q^2, shows a different pattern: a strong energy dependence of the cross section, values of b consistent with a point-like γ V vertex, and the restoration of the SU(4)

flavor symmetry, that indicate a type of dynamic consistent with pQCD predictions.

- Photon diffraction at large Q^2shows a value of $\alpha_{I\!P}$ only slightly higher than the values obtained in photoproduction, indicating that the same mechanism used to explain photoproduction processes can be used to explain a large fraction of diffractive dissociation at high Q^2. The partonic structure of the Pomeron has been measured and found to be dominated by hard gluons. Factorization has been found to be valid within the current sensitivity and measurements range.

Acknowledgements

It is a pleasure to thank H. Abramovich, M. Arneodo, J. Dainton, E. Gallo, G. Iacobucci, A. Levi, R. Nania, J. Phillips, F. Sciulli, A. Solano, and also thanks to Lilian DePorcel for her infinite patience and understanding.

References

[1] H1 Collaboration, DESY 93-103.

[2] ZEUS Collaboration, The ZEUS Detector, Status Report (1993).

[3] G. Iacobucci, talk given at the 1996 Zeuthen Workshop on Elementary Particle Theory, Rheinsberg, Germany (1996);
A. Staiano, talk given at Les Rencontres de la Physique de la Valle d'Aoste, La Thuile (1996);
G. Barbagli, talk given at the 1996 IHEP Conference, Warsaw.

[4] P. D. B. Collins, *An Introduction to Regge Theory and High Energy Physics*, (Cambridge University Press, Cambridge, 1977).

[5] M. Perl, *High Energy Hadron Physics*, (Wiley & Sons, New York, 1974).

[6] A. Donnachie, P. V. Landshoff, Phys. Lett. **B 296**, 227 (1992).

[7] H1 Collaboration, S. Aid *et al.*, Z. Phys. **C 69**, 27 (1995).

[8] ZEUS Collaboration, M. Derrick et al., Z. Phys.**C 63**, 391 (1994).

[9] CDF Collaboration., F. Abe *et al., Phys. Rev.**D50**, 5550 (1994)* .

*[10] H. Abramowicz et al., Phys. Lett.**B269**, 465 (1991).*

[11] ZEUS Collaboration, M. Derrick et al., DESY 96-076 (June 1996).

*[12] H1 Collaboration, F. Abe et al., Nucl. Phys.**B 470** (1996).*

[13] M. Ryskin et al., Proceedings of the workshop "Physics at HERA", 'Heavy photon dissociation in DIS', (Hamburg, 1991).

[14] B. Kopeliovich et al., hep-ph/9601291.

*[15] J. D. Bjorken, Phys. Rev.**D 47**, 101 (1992).*

[16] M. Przybycien et al., hep-ph/9606294.

*[17] A. Donnachie, P. V. Landshoff, Nucl. Phys.**B 244**, 322 (1984).*

*[18] A. Donnachie, P. V. Landshoff, Phys. Lett.**B 191**, 309 (1987).*

*[19] G. Ingelman and P. Schlein, Phys. Lett.**B 152**, 256 (1985).*

*[20] N. N. Nikolaev, B. G. Zakharov, Phys. Lett.**B 260**, 414 (1991).*

[21] H. Abramowicz et al., Proceedings of the 1994 SLAC Summer Inst., 539 (1994).

*[22] N. Nikolaev et al., Z. Phys.**C 53**, 331 (1992).*

[23] E. Gotsman et al., hep-ph/9606280.

*[24] E. Levin et al., Phys. Rev.**D 50**, 4306 (1994).*

*[25] M. Genovese et al., Sov. Phys. JEPT**81**, 625 (1995).*

*[26] M. Genovese et al., Phys. Lett.**B 380**, 213 (1996).*

[27] J. Bjorken, AIP Conference Proceedings No. 6, Particles and Fields Subseries N0. 2, edited by M. Bander, G. Shaw, and D. Wong (AIP, New York, 1972);
*J. D. Bjorken and J. Kogut, Phys. Rev.**D 8**, 1341 (1973);*
J. D. Bjorken, preprint SLAC-PUB-7096 (1996), hep-ph/9601363.

*[28] W. Buchmuller et al., Phys. Lett.**B355**, 573 (1995).*

[29] R. Feynman, Photon-Hadron Interactions, (Addison-Wesley, 1989).

*[30] M. G. Ryskin, Z. Phys.**C 57**, 89 (1993).*

*[31] S.J. Brodsky et al., Phys. Rev.**D50**, 3134 (1994).*

*[32] J. Nemchik et al., Phys. Lett.**B 341**, 228 (1994).*

[33] A. D. Martin et al.hep-ph/9609448.

[34] ZEUS Collaboration, M. Derrick et al., Phys. Lett. ***B 356****, 601 (1995).*

[35] H1 Collaboration, F. Abe et al., Nucl. Phys. ***B 463****, 3 (1996).*

[36] ZEUS Collaboration, M. Derrick et al., DESY 96-183, accepted by Z. Phys. - MS 418.

[37] ZEUS Collaboration, M. Derrick et al., Z. Phys. ***C 69****, 39 (1995).*

[38] H1 Collaboration, F. Abe et al., Nucl. Phys. ***B 468****, 3 (1996).*

[39] ZEUS Collaboration, M. Derrick et al., Phys. Lett. ***B 377****, 259 (1996).*

[40] ZEUS Collaboration, M. Derrick et al.,Phys. Lett. ***B 380****, 220 (1996).*

[41] H1 Collaboration, F. Abe et al., Phys. Lett. ***B 338****, 507 (1994).*

[42] ZEUS Collaboration, M. Derrick et al., Phys. Lett. ***B 350****, 120 (1995).*

[43] H1 Collaboration, F. Abe et al., Nucl. Phys. ***B 472****, 3 (1996).*

[44] ZEUS Collaboration, M. Derrick et al., ICHEP 1996, pa 02-051.

[45] ZEUS Collaboration, M. Derrick et al., ICHEP 1996, pa 02-053.

[46] ZEUS Collaboration, M. Derrick et al., ICHEP 1996, pa 02-028.

[47] H1 Collaboration, F. Abe et al., ICHEP 1996, pa 02-064.

[48] H1 Collaboration, F. Abe et al., ICHEP 1996, pa 02-085.

[49] ZEUS Collaboration, M. Derrick et al., ICHEP 1996, pa 02-049.

[50] H1 Collaboration, F. Abe et al., ICHEP 1996, pa 02-086.

[51] H1 Collaboration, F. Abe et al., ICHEP 1996, pa 01-088.

[52] CDF Collaboration, F. Abe, et al., Phys. Rev. ***D 50****, 5535 (1994), 855 (1995).*

[53] A. Schiz et al., Phys. Rev. ***D 24*** *(1981) 26.*

[54] A. Staiano, "Silicon detectors for the leading proton spectrometer of ZEUS," proceedings of the Third International Workshop on Vertex Detectors, IUHEE-95-1;
K. O'Shaughnessy et al., Nucl. Instrum. Methods ***A 342****, 260-263 (1994*

[55] L. Frankfurt et al., Phys. Rev. ***D 54****, 3194 (1996).*

[56] N. N. Nikolaev et al., Phys. Lett. ***B 366****, 337 (1996).*

[57] H. Abramowicz et al.Proceeding of "Future Physics at HERA", Hamburg, 1996.

[58] ZEUS Collaboration, M. Derrick et al., Phys. Lett. ***B 315****, 481 (1993).*

[59] ZEUS Collaboration, M. Derrick et al., Z. Phys. ***C 70****, 391 (1996).*

[60] K. Goulianos, Phys. Rep. ***101****, 169 (1983).*

[61] H1 Collaboration, F. Abe et al., ICHEP 1996, pa 02-067.

[62] ZEUS Collaboration, M. Derrick et al., ICHEP 1996, pa 02-048.

[63] ZEUS Collaboration, M. Derrick et al., Z. Phys. ***C 67****, 227 (1995).*

[64] H1 Collaboration, F. Abe et al., ICHEP 1996, pa 02-061.

[65] ZEUS Collaboration, M. Derrick et al., ICHEP 1996, pa02-026.

[66] A.H. Mueller, Phys. Rev. ***D 2****, 2963 (1970); ibid.* ***D 4****, 150 (1971).*

[67] R.D. Field and G. Fox, Nucl. Phys. ***B 80****, 367 (1974).*

[68] H1 Collaboration, F. Abe et al., Phys. Lett. ***B 348****, 681 (1995).*

[69] ZEUS Collaboration, M. Derrick et al., Z. Phys. ***C 68****, 569 (1995).*

[70] P. V. Landshoff, talk given at the International Workshop on Deep Inelastic Scattering and Related Phenomena (DIS 96), Rome, Italy, 15-19 Apr. 1996, hep-ph/9605331

[71] J. B artels et al., Phys. Lett. ***B379****, 239 (1996), ERRATUM-ibid.* ***B 382****, 449 (1996).*

[72] Yu. L. Dokshitzer, JETP ***46****, 641 (1977).*
V. N. Gribov and L. N. Lipatov, Sov. J. Nucl Phys. ***15****, 78 (1972).*
G. Altarelli and G. Parisi, Nucl. Phys. ***B 126****, 298 (1977).*

[73] ZEUS Collaboration, M. Derrick et al., Phys. Lett. ***B 356****, 129 (1995).*

[74] ZEUS Collaboration, M. Derrick et al., ICHEP 1996, pa 02-039.

[75] H1 Collaboration, F. Abe et al., ICHEP 1996, pa 02-068.

[76] P. Bruni and G. Ingelman, DESY 93-187.

[77] PYTHIA 5.6: H.-U. Bengtsson and T. Sjöstrand, Comp. Phys. Comm. ***46****, 43 (1987).*

[78] Y. Dokshitzer, V. Khoze and S. Troyan, in Proceedings of the 6th International Conference on Physics in Collisions, Chicago, Illinois, edited by M. Derrick (World Scientific, Singapore, 1987) p. 417.

[79] D0 Collaboration, S. Abachi et al., Phys. Rev. Lett. ***72****, 2332 (1994);*
D0 Collaboration, S. Abachi et al., FERMILAB-PUB-95-302-E (1995).

[80] CDF Collaboration, F. Abe, et al., Phys. Rev. Lett. ***74****, 855 (1995).*

[81] V. Del Duca and W.-K. Tang, Phys. Lett. ***B 312****, 225 (1993).*

[82] ZEUS Collaboration, M. Derrick et al., Phys. Lett.B369, 55 (1996).

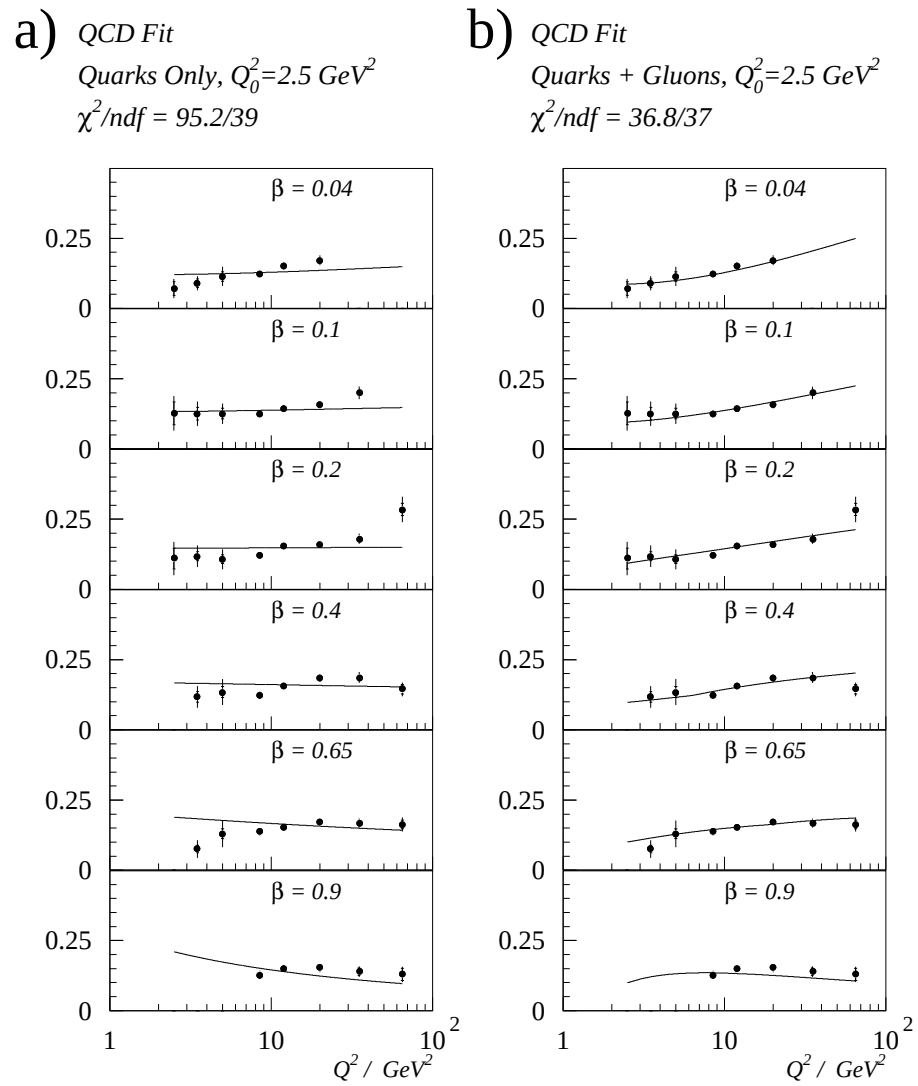

Figure 29: DGLAP QCD comparison of the (β, Q^2) dependence of $\tilde{F_2^D}$: (a) assuming only quarks at the starting scale of $Q_0^2 = 2.5$ GeV^2, (b) assuming both quarks and gluons at the starting scale of $Q_o^2 = 2.5$ GeV^2.

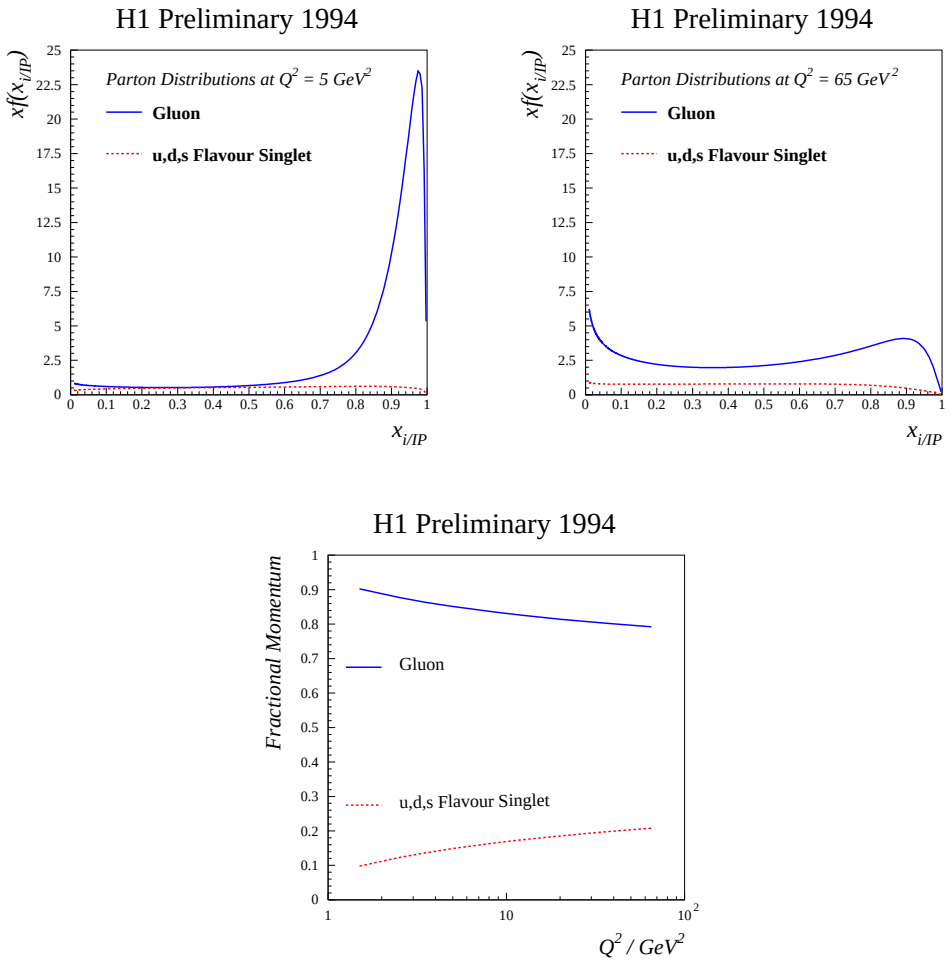

Figure 30: Quark and gluon fractional momentum distributions for diffractive exchange averaged over x_{IP} and t extracted using the DGLAP QCD fit at (a) Q^2= 5 GeV^2 and (b) Q^2= 65 GeV^2; (c) fraction of the total momentum carried by quarks and by gluons as a function of Q^2.

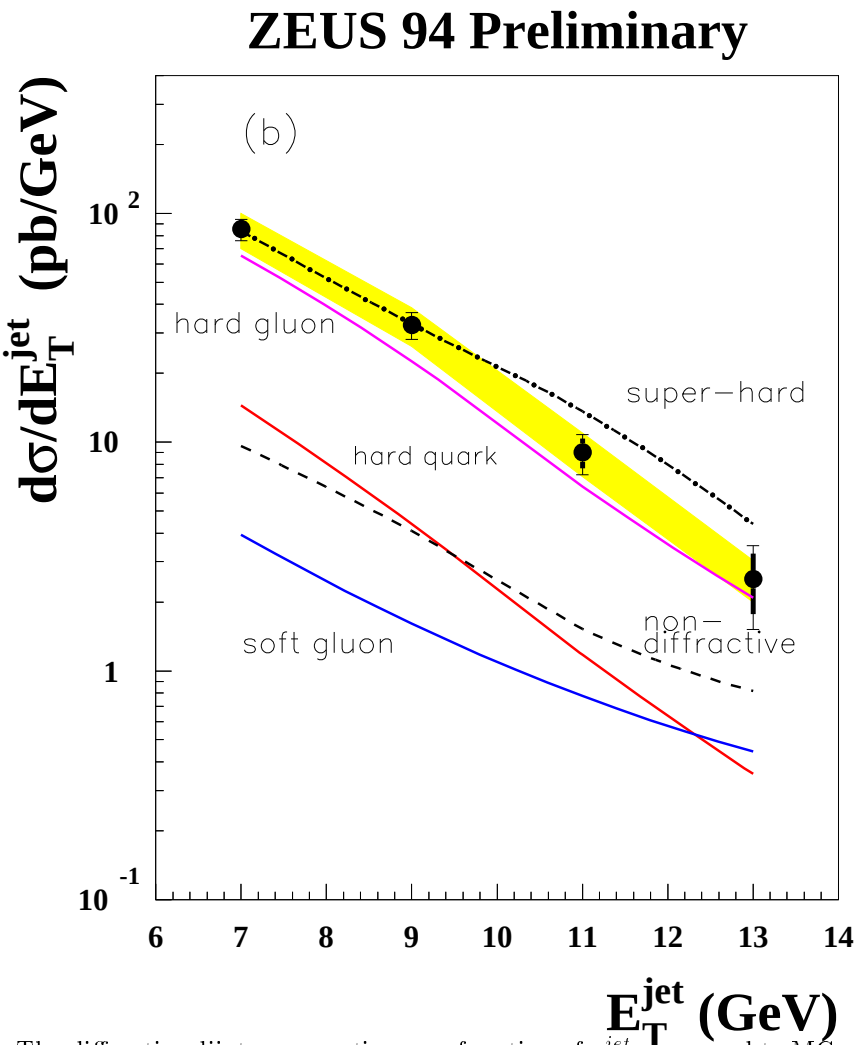

Figure 31: The diffractive dijet cross section as a function of η^{jet} compared to MC predictions for different Pomeron momentum densities.

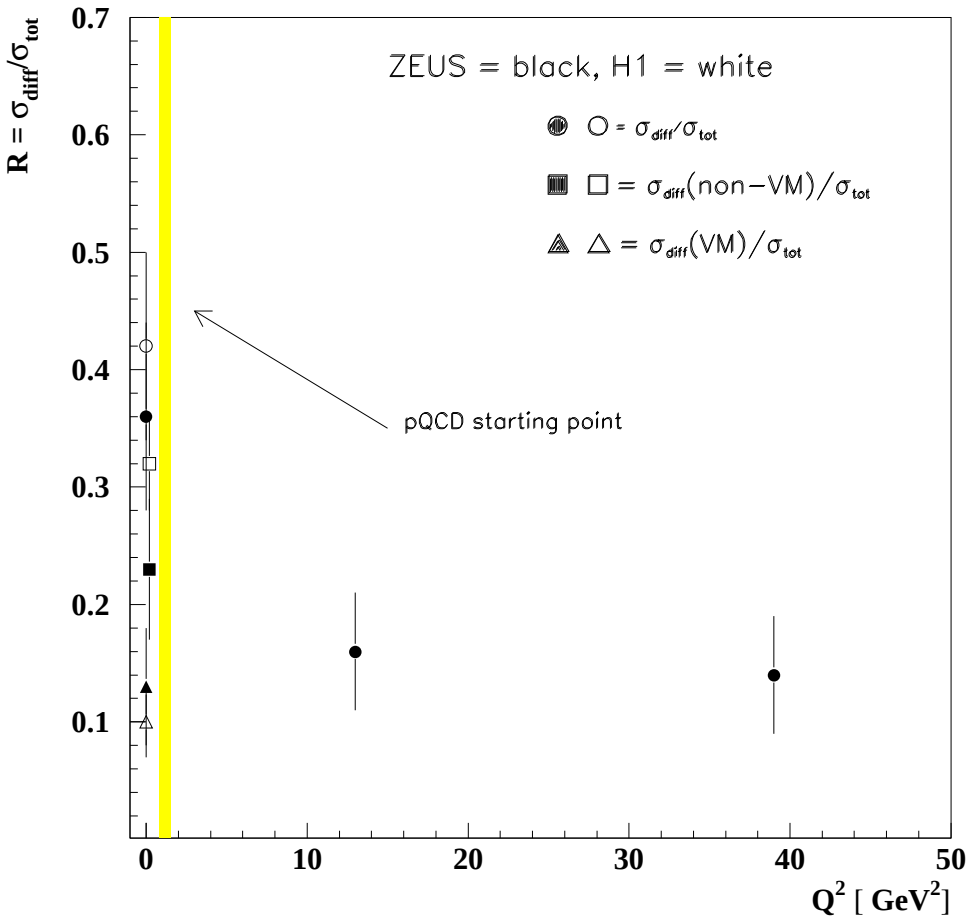

Figure 32: Ratio between the diffractive and total cross section as a function of Q^2.

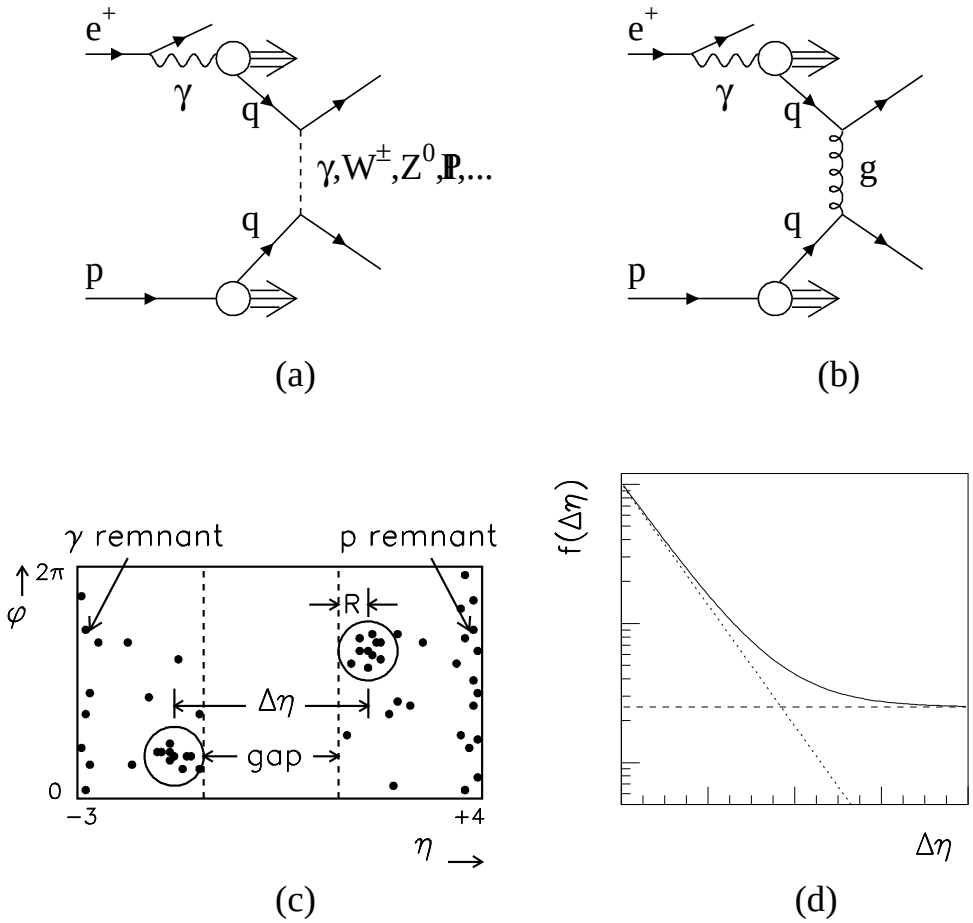

Figure 33: Resolved photoproduction via (a) color singlet exchange and (b) color non singlet exchange. The rapidity gap event morphology is shown in (c), where black dots represent final state hadrons and the boundary illustrates the limit of the ZEUS acceptance. Two jets of radius R are shown, which are back-to-back in azimuth and separated by a pseudorapidity interval $\Delta\eta$. An expectation for the behavior of the gap fraction is shown in (d)(solid line). The non singlet contribution is shown as the dotted line and the color singlet contribution as the dashed line.

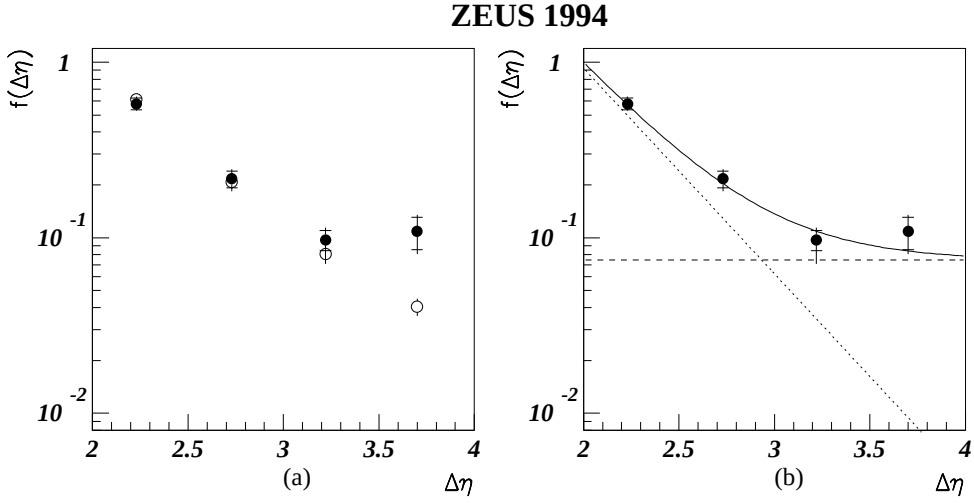

Figure 34: Results from events with central rapidity gaps. (a) Points before (open circles) and after (full circles) detector corrections. (b) Fit as explained in the text.